Convergent evolution of noxious heat sensing by TRPA5, a novel class of heat sensor in *Rhodnius prolixus*

Marjorie A. Liénard[1,2,3*], David Baez-Nieto[4*], Cheng-Chia Tsai[5], Wendy A. Valencia-Montoya[2], Balder Werin[6], Urban Johanson[6], Jean-Marc Lassance[2,7], Jen Q. Pan[4], Nanfang Yu[5], Naomi E. Pierce[2]

[1]Department of Biology, Lund University, Lund, Sweden

[2]Department of Organismic and Evolutionary Biology and Museum of Comparative Zoology, Harvard University, Cambridge, MA 02138, USA

[3]Broad Institute, Cambridge, MA 02142, USA

[4]Stanley Center for Psychiatric Research, Broad Institute, Cambridge, MA 02142, USA

[5]Department of Applied Physics and Applied Mathematics, Columbia University, New York, NY 10027, USA

[6]Division of Biochemistry and Structural Biology, Department of Chemistry, Lund University, Lund, Sweden

[7]GIGA-Research, University of Liège, Liège, Belgium

[*] These authors contributed equally to the work

ORCIDs:

MAL:0000-0003-3193-3666

DBN:0000-0002-2238-8486

CCT:0000-0001-5662-6908

WAVM:0000-0001-9246-2330

BW:0009-0006-1188-3496

UJ: 0000-0001-8862-128X

JML: 0000-0002-3675-6956

JQP: 0000-0003-0767-086X

NY:0000-0002-9462-4724

NEP:0000-0003-3366-1625

Correspondence:

marjorie.lienard@biol.lu.se

Keywords: transient receptor potential channel, temperature, noxious heat, insect vector, patch-clamp recordings, triatomine, Chagas disease, convergent evolution

ABSTRACT

Insects are ectotherms, and as such, rely on a diverse repertoire of thermoreceptors to monitor environmental temperature and control behavioral thermoregulation. Here, we use structural, phylogenetic, genetic, and functional analyses to show that TRPA5 genes, widespread across numerous insect orders, encode a novel class of noxious heat receptors. We show that in the triatomine bug *Rhodnius prolixus*, the primary vector of Chagas disease, Rp-TRPA5$_2$ differs biophysically and structurally from noxious thermoTRPAs previously described in insects. This includes key changes in the ankyrin repeat domain and the selectivity filter of the channel. *In vitro*, we find evidence that the homo-tetrameric channel is not activated by voltage, but displays high thermosensitivity with an enthalpy change (ΔH) of 72 kcal/mol associated with the channel activation, with a Q_{10} = 25 and $T°_{half}$ = 58.6°C. Structural analyses reveal parallels in the overall ion channel architecture between fruit fly TRPA1 and Rp-TRPA5$_2$; however, functional properties and expression patterns indicate that the role of Rp-TRPA5$_2$ is more similar to that of *Pyrexia* noxious heat receptors found in fruit flies. *Pyrexia* genes have been lost in true bugs, and our findings suggest that the rapidly evolving insect TRPA gene family has given rise to an independent evolutionary origin of a molecular transducer that is responsive to noxious thermal stimuli.

Introduction

Animal thermosensation is critical for performance in fluctuating environments. Changes in environmental temperature are transduced by the sensory system as part of physiological feedback controlling responses such as metabolic homeostasis, feeding, finding suitable habitats, and extreme-heat avoidance [1, 2]. At the molecular level, thermal perception is mediated by the temperature-dependent activation of specific cold- and heat-activated receptors [3, 4]. Although families such as ionotropic receptors (IRs) and gustatory receptors (GRs) have been linked to peripheral innocuous thermosensation in insects [3-6], the transient receptor potential (TRP) receptor family encodes the greatest diversity of thermosensitive channels. TRP receptors are remarkably diverse (TRPA, TRPC, TRPN, TRPM, TRPML and TRPV) and play salient roles as polymodal ion channels responding to chemical, mechanical, and thermal stimuli [7-12].

Mammalian TRP channels involved in temperature detection (thermoTRPs) belong to the TRPA, TRPV and TRPM subfamilies (Table 1) and are activated by temperatures from noxious cold to noxious heat [4, 9, 13-16]. In invertebrates, known thermoTRP channels have so far been restricted to the ankyrin TRPA subfamily of genes including *Painless*, *Pyrexia*, *TRPA1*, and *Hs-TRPA* (Fig. 1; Fig. S1) [11, 12]. In *Drosophila melanogaster, Painless*, *Pyrexia* and *Dm-TRPA1* isoforms A, B and D encode receptors that exhibit distinct biophysical properties, cellular expression patterns and temperature activation thresholds ranging from 19°C to 46°C [17-24]. TRPA1 is also a heat–activated TRP sensor in *Anopheles gambiae* (25-37°C), and other mosquitos [25, 26], playing a key role in tuning heat-seeking behavior. Outside the Diptera, TRPA1 has been characterized as a heat-sensitive channel in other insects as it is known to regulate the induction of embryonic diapause in *Bombyx mori* at temperatures above 21°C [27]. The subfamily *Waterwitch* includes receptors responding to stimuli in different modalities from ancestral hygrosensation found in fruit flies [20] to derived heat sensing exhibited by hymenopterans and mediated by the Hs-TRPA subfamily, which diverged following a duplication from *Waterwitch* [12]. Thus, despite the loss of TRPA1 in Hymenoptera, in honeybees, *Apis mellifera* Am-HsTRPA responds to temperatures around 34°C, in parasitoid wasps, *Nasonia*

vitripennis Nv-HsTRPA activates in response to small temperature differences in the range 8°C to 44°C regardless of initial temperatures, and in fire ants, *Solenopsis invicta,* Si-HsTRPA is activated in the range 28-37°C [28, 29]. Notably, the insect TRP ankyrin family has an additional subfamily of unknown function, TRPA5, which is seemingly absent from the fruit fly genome yet found across several other orders of insects [11].

Here we deorphanize and characterize an ankyrin TRPA5 ion channel from the “kissing” bug, *Rhodnius prolixus*. Long used as a model organism in studies of insect development and physiology [30], *R. prolixus* (Hemiptera, Reduviidae: Triatominae) has become increasingly relevant for molecular and functional studies. This is primarily explained by its long-term medical and societal impact as a haematophagous vector of *Trypanosoma cruzi*, the causative agent of Chagas’ disease [31]. Due to the progressive adaptation of wild triatomine vector species to domestic environments, vector transmission to human populations has increased in recent years [32, 33]. The disease currently affects over 8 million people worldwide, with vector transmission causing around 30,000 new cases yearly [32, 34, 35]. Extensive long-term efforts towards decoding the sensory ecology of triatomines [36-38] have identified olfactory, thermal and environmentally-mediated cues as well as the neuroethology underlying its complex host-seeking behavior [38-45]. Moreover, the annotated *R. prolixus* genome [37] and recent transcriptomic studies [44-46] provide detailed expression profiles of candidate sensory receptor genes, including olfactory, ionotropic, pickpocket, and transient receptor potential receptors that can be used to probe the genetic basis of sensory traits [47, 48].

In this study, we leverage the rich genomic and transcriptomic resources available for *R. prolixus* along with molecular, structural modeling and functional approaches to characterize a TRPA5 ion channel enriched in canonical sensory tissues. The biophysical properties of the ion channel demonstrate that *TRPA5* encodes a novel ankyrin type of heat-activated TRP receptor responding to noxious temperatures. Analyses of predicted structures reveal that the channel displays unique features among the ankyrin family, potentially affecting its ion conduction properties despite sharing

conserved structural domains with other ankyrin thermoTRPs. These findings may facilitate future studies of agonist responses of TRPA5 to assist in the development of novel genetic tools for vector control efforts.

97 **Table 1**. Vertebrate and invertebrate TRP ion channels involved in thermal transduction.

Nomenclature	Other names	Organism	Expression	TRP family	Thermal treshold*	Activity range	Entropy change (ΔS) cal/mol*K	Activation enthalpy (ΔH) kcal/mol	Q10**	Reference
Vertebrate transient receptor potential (TRP) channels involved in thermosensation										
TRPV1	Vr1	*Rattus norvegicus* (rat), *Homo sapiens* (human)	nociceptor neurons	Ankyrin	≥ 42℃ (40-45)		260 (at 30mV)	90-100	16.8, 20*	Caterina et al 1997, Cheng et al 2012*, Yao et al 2010*
TRPV1(l)	TRPV1- long	*Desmodus rotundus* (vampire bat)	DRG and TG neurons	Ankyrin	40℃				12	Gracheva et al. 2011
TRPV1(s)	TRPV1- short	*Desmodus rotundus* (vampire bat)	TG neurons	Ankyrin	30℃				5	Gracheva et al. 2011
TRPV2	Vrl2	*Rattus norvegicus* (rat), *Homo sapiens* (human)	nociceptor neurons	Ankyrin	≥ 52℃ (50-53)		586	200	20.6	Caterina et al 1999
hTrpv3	Vrl3	*Homo sapiens* (human)	skin keratinocytes	Ankyrin	≥ 33℃ (34-38℃)	33℃~50℃ (Max 41-47℃)	n.d		6.62	Peier et al 2002; Smith et al 2002
hTrpv4	OTRPC4, VR-OAC, Trp12, Vrl2	*Homo sapiens* (human)	skin and dorsal root ganglion neurons	Ankyrin	~ 27-34℃		n.d		9.9+/-3.8	Güler et al 2002; Watanabe et al 2002
TRPM8	CMR1			Melastatin	≤ 23-25℃	0℃-25℃	-384	-112	24	McKemy et al 2002; Brauchi et al 2004;
TRPM3		*Mus musculus* (mouse)	DRG and TG sensory neurons	Melastatin	≥ 43℃				7.2	Vriens et al 2011
TRPC5		*Mus musculus* (mouse), *Homo sapiens* (human)	DRG neurons	Canonical	<37℃->25℃		n.d.	-40		Zimmermann et al 2011
Anktm1	TRPA1	*Mus musculus* (mouse), *Homo sapiens* (human)	DRG neurons	Ankyrin	≤ 17℃	0℃-17℃	-140	-40	6	Story et al 2003
Chicken TRPA1	TRPA1	*Gallus gallus domesticus* (chicken)	DRG neurons	Ankyrin	39.4℃					Saito et al 2014
xtTRPA1	TRPA1	*Xenopus tropicalis* (Western clawed frog)	DRG neurons	Ankyrin	39.7℃				59.24+/-18	Ohkita et al 2012
xlTRPA1	TRPA1	*Xenopus laevis* (African clawed frog)	DRG neurons	Ankyrin	36.2 +/-0.4℃					Saito et al. 2016
snTRPA1	TRPA1	*Crotalus atrox* (rattlesnake)	TG neurons	Ankyrin	27.6℃				13.7	Gracheva et al. 2010
python TRPA1	TRPA1	*Python regius* (python)	TG neurons	Ankyrin	32.7℃				n.d.	Gracheva et al. 2010
boa TRPA1	TRPA1	*Corallus hortulanus* (boa)	TG neurons	Ankyrin	29.6℃				n.d.	Gracheva et al. 2010
ratsnake TRPA1	TRPA1	*Elaphe obsoleta lindheimeri* (rat snake)	TG neurons	Ankyrin	37.2℃				8.8	Gracheva et al. 2010
Anole TRPA1	TRPA1	*Anolis carolinensis* (green anole)	TG neurons	Ankyrin	33.9℃				45.71+/-6	Saito et al. 2012
A. allogus TRPA1	TRPA1	*Anolis allogus*	Dorsal skin	Ankyrin	33.5 +/-0.7℃					Akashi et al. 2018
A. homolechis TRPA1	TRPA1	*Anolis homolechis*	Dorsal skin	Ankyrin	36.4 +/-0.8℃					Akashi et al. 2018
A. sagrei TRPA1	TRPA1	*Anolis sagrei*	Dorsal skin	Ankyrin	33.5 +/-0.7℃					Akashi et al. 2018
axTRPA1	TRPA1	*Ambystoma mexicanum* (axolotl)	Brain, lung, heart, stomach	Ankyrin	39.7 +/-1.0℃					Oda et al. 2019
*zTRPA1b****	TRPA1	*Danio rerio* (zebrafish)	Sensory neurons innervating skin and cranial sensory ganglia	Ankyrin	variable < 10℃ (cold); > 25℃ (heat)				8.2+/-0.6	Oda et al. 2016
olTRPA1	TRPA1	*Oryzias latipes* (medaka)		Ankyrin	variable					Oda et al. 2017
trTRPA1	TRPA1	*Takifugu rubripes* (pufferfish)		Ankyrin	variable < 8℃ (cold); > 25℃ (heat)					Oda et al. 2018

Invertebrate transient receptor potential (TRP) channels involved in thermosensation										
*ceTRPA1******		*Caenorhabditis elegans* (nematode)	neurons, muscle, intestine, and epithelial cells		≤ 17℃					Reviewed in Laursen et al. 2015
Painless	dAnktm1	*Drosophila melanogaster* (fruit fly)		Ankyrin	~39-42℃					Tracey et al 2003; Sokabe et al. 2008
Pyrexia	Pyx-PA and Pyx-PB	*Drosophila melanogaster* (fruit fly)	embryos: peripheral nerves and central nerves, multidendritic neurons in larval epidermis;adults: sensory neurons around bristle eyes, britsle neurons along thorax, neurons in maxillary palps, proboscis, antennae	Ankyrin	≥ 40 ℃				Pyx-PA 18.145; Pyx-PB 15.329	Lee et al. 2005; Neely et al. 2011
dTRPA1(A)	TrpA1-RI (Prom B, ex10a), dTrpA1, dANKTM1, DmTRPA1	*Drosophila melanogaster* (fruit fly)	larval sensory neurons, adult proboscis	Ankyrin	27-29℃				9	Viswanath et al. 2003; Rosenzweig et al. 2005; Hamada et al 2008; Kang et al. 2012
dTRPA1(D)	TrpA1-RG (Prom A, ex10a), dTrpA1, dANKTM1, DmTRPA1	*Drosophila melanogaster* (fruit fly)	larval nociceptors	Ankyrin	≥ 46 ℃				116	Zhong et al. 2012
AgTRPA1		*Anopheles gambiae* (African malaria mosquito)	antennae, head	Ankyrin	25.2℃					Wang et al. 2009
AsTRPA1(A)		*Anopheles stephensi* (Asian malaria mosquito)	antennae, head	Ankyrin	30.3 +/- 0.9℃				14,5	Li et al. 2019
AaTRPA1(B)		*Aedes aegypti* (yellow fever mosquito)	antennae, head	Ankyrin	32 +/- 0.8℃				20,7	Li et al. 2019
CpTRPA1(A)		*Culex pipiens pallens* (northern house mosquito)	antennae, head	Ankyrin	21.8 +/- 0.7℃				61,2	Li et al. 2019
TRPA1		*Bombyx mori* (silk moth)		Ankyrin	21.6℃				20,5	Sato et al. 2014
hsTRPA	AmhsTRPA	*Apis mellifera* (honeybee)	antennae	Ankyrin	33.9 +/-0.6℃				17.2+/-4.0	Kohno et al. 2010
Rp-TRPA5$_2$	Rp-TRPA5B	*Rhodnius prolixus* (kissing bug)	head, rostrum, legs, antennae	Ankyrin	53℃; Thalf 58.6℃	53-68℃	274	72	25	*this study*

* Activation threshold temperature as determined in heterologous expression systems
** Q10 is the fold current increase over 10 ℃ increase as a measure of sensitivity, the higher Q10 value, the more sensitivity to heat the channel

98

Results and discussion

TRPA5 genes are ancient ankyrin receptors found across many insect orders but lost in Diptera

To start investigating the molecular basis of thermosensation in Rhodnius, we first reanalyzed the genome annotations (Version RproC3.3) complemented with available transcriptomic resources (*see Methods*) to gain insights into gene variation and genomic architecture within the TRP ankyrin family. Genomes of triatomines [37] and additional surveyed hemipteran species (Table S1) all lack an ortholog to *Pyrexia* (*Pyx*) TRP but possess one gene copy of the three canonical ankyrin TRP genes: *Waterwitch* (*Wtrw*), *TRPA1* and *Painless* (*Pain*) (Fig. 1A, Fig. S1). Rhodnius *TRPA1* and *Painless* exhibit a wide mRNA tissue distribution (Fig. 1B) that potentially indicates a canonical role in thermosensation, similarly to TRPAs expression patterns in other insect species [27-29, 49].

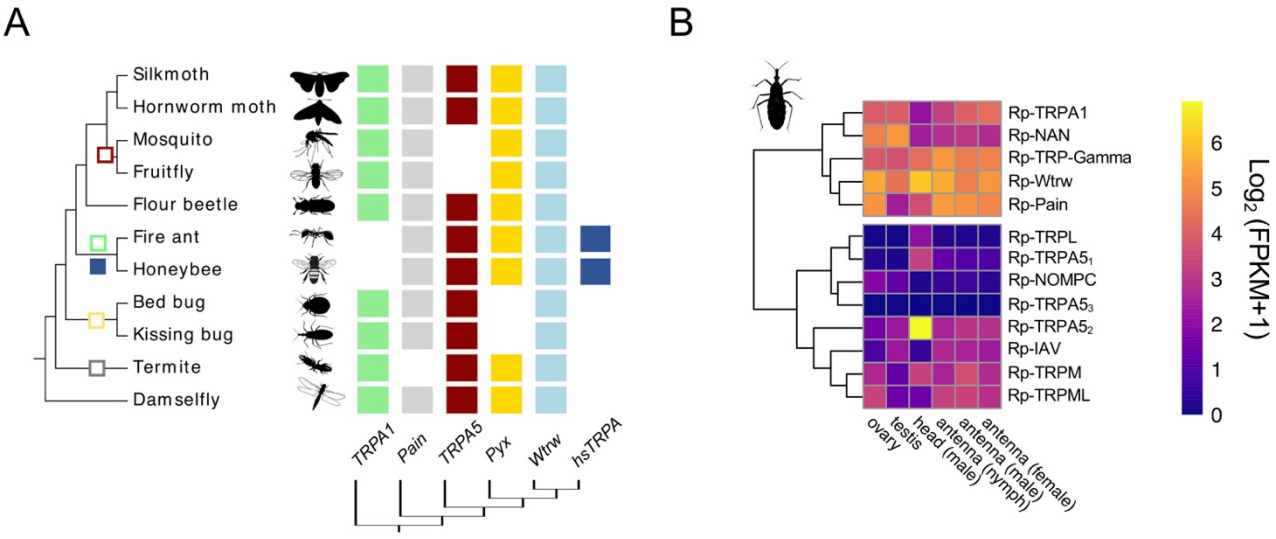

Figure 1. A. Phylogenetic reconstruction of the ankyrin TRP (TRPA) channel family in representative insect species. TRPA5 channels are present across insect Orders but absent from dipteran genomes (see also Fig. S1 and S2). Gene abbreviations: *Painless (Pain), Pyrexia (Pyx), Waterwitch (Wtrw*), hymenopteran-specific TRPA (*hsTRPA*). Silkmoth, *Bombyx mori*; Hornworm moth, *Manduca sexta*; Mosquito, *Anopheles gambiae*; Fruit fly, *Drosophila melanogaster*; Flour beetle, *Tribolium castaneum*; Fire ant, *Solenopsis invicta*; Honeybee, *Apis mellifera*; Bed bug, *Cimex lectularis;* Kissing bug*, Rhodnius prolixus*; Termite, *Zootermopsis nevadensis*; Bluetail Damselfly, *Ischnura elegans.* **B.** Phylogenetic relationships of TRP genes in *R. prolixus* and their corresponding

expression levels across tissues in published transcriptomic data. Heat maps compare the expression levels across tissues and developmental stages. Expression levels are represented as Log_2 FPKM +1 and depicted with a gradient color scale. Gene models are based on genomic annotations [37], *de novo* transcriptome assembly [44] and manual annotation of gene models not annotated in the two aforementioned studies (see *Methods*).

Our scaffold-mapping analysis of three *TRPA5* isoforms previously annotated in *R. prolixus* [37] shows that the predicted-isoforms A and B map to different genomic locations, and consist of two physically close tandem-duplicate loci, whereas predicted-isoform C maps to a distinct scaffold. Therefore, TRPA5A, TRPA5B and TRPA5C are hereafter referred to as three distinct loci, $TRPA5_1$, $TRPA5_2$, and $TRPA5_3$. Intrigued by the finding of multiple *TRPA5* gene copies, we performed an extensive *TRPA5* gene search across annotated genomic and transcriptomic datasets available for the insect Orders Anoplura, Diptera, Coleoptera, Hemiptera, Hymenoptera, Isoptera, Lepidoptera, Odonata and Thysanoptera. Our phylogenetic reconstruction shows that the TRPA5 ankyrin subfamily is completely absent in all surveyed dipteran genomes (Fig. S2). TRPA5 orthologs were nonetheless found spanning the orders Lepidoptera, Coleoptera, Hymenoptera, Hemiptera, Isoptera and Odonata (Fig. S2), including remarkable group-specific expansions such as those in the fire ant, *Solenopsis invicta* [29], the damselfly *Ischnura elegans*, the tobacco hornworm moth *Manduca sexta*, and several hemipterans (Fig. S2). In addition to lineage-specific expansions through duplications, complex alternative splicing also seems to play a role in TRPA5 functional diversification [50]. Altogether, our large-scale phylogenetic analyses recapitulate that the insect TRPA ankyrin family comprises five rapidly evolving clades consisting of *Waterwitch* (and HsTRPA1), *Pyrexia* (presumably lost in Hemiptera), *TRPA5* (presumably lost in Diptera), *TRPA1* and *Painless* (Fig. 1A, SI File 1, Table S1).

Prior to interrogating a possible role for Rhodnius TRPA5 in thermosensation, we asked whether these TRPs are expressed in sensory tissues. Whereas Rp-$TRPA5_1$ and Rp-$TRPA5_3$ mRNAs are expressed at low or below detection thresholds across tissues (Fig. 1B), Rp-$TRPA5_2$ mRNA appears to be the most abundant TRPA5 transcript in adult Rhodnius. Rp-$TRPA5_2$ is significantly enriched in adult male

and female heads (Fig. 1B, Fig. S3, Table S5). We further examined expression profiles of Rp-TRPA5$_2$ via quantitative PCR of additional canonical sensory tissues. Rp-TRPA5$_2$ is abundant in the rostrum and legs and expressed at lower levels in antennae (Fig. 1B, Fig. S3), a first indication in line with a possible role in thermosensation.

Rhodnius TRPA5$_2$ exhibits unique structural features in the Ankyrin Repeat Domain and the selectivity filter

To visualize structural features of Rhodnius ankyrin TRP homologs, we used DeepMind's protein structure prediction software AlphaFold 2.0 [51-53]. Monomeric structures of Rhodnius TRPA1, Painless, Waterwitch, and TRPA5$_2$ were modeled, as well as a tetrameric model of the Rhodnius TRPA5$_2$. We then performed pairwise comparisons of the Rhodnius orthologs to their Drosophila correspondent monomeric structures for TRPA1, Painless and Waterwitch, and compared Rp-TRPA5$_2$ to Dm-Pyx separately (Fig. 2). Each monomeric prediction is presented using a coloring scheme reflecting a structural reliability measure (Fig. 2A) next to a rainbow representation running from the N- to the C-terminus (Fig. 2B).

All Rhodnius and Drosophila ankyrin TRP monomeric structures shared several expected features with the cryo-EM structure of HsTRPA1 [54], including the N-terminal ankyrin repeat domain (ARD), six transmembrane α-helices (S1-S6), and a region corresponding to the allosteric nexus of Hs-TRPA1 connecting the ARD and the transmembrane region [54]. The C-terminal region features at least one α-helix, which together with the corresponding helices from the other subunits, most likely form a coiled-coil in the tetramer as seen in the solved TRPA1 structures. Furthermore, the recently published structure of Dm-TRPA1-A in state 1 confirms distinct predicted features in our model, including the interfacial helix and the interaction between AR12 and the region C-terminal of the coiled-coil helix [55]. However, without the constraints of the other monomers and the interactions that would force the C-terminus into the coiled-coil, some of the helices are oriented in unrealistic directions while the secondary structure remains plausible.

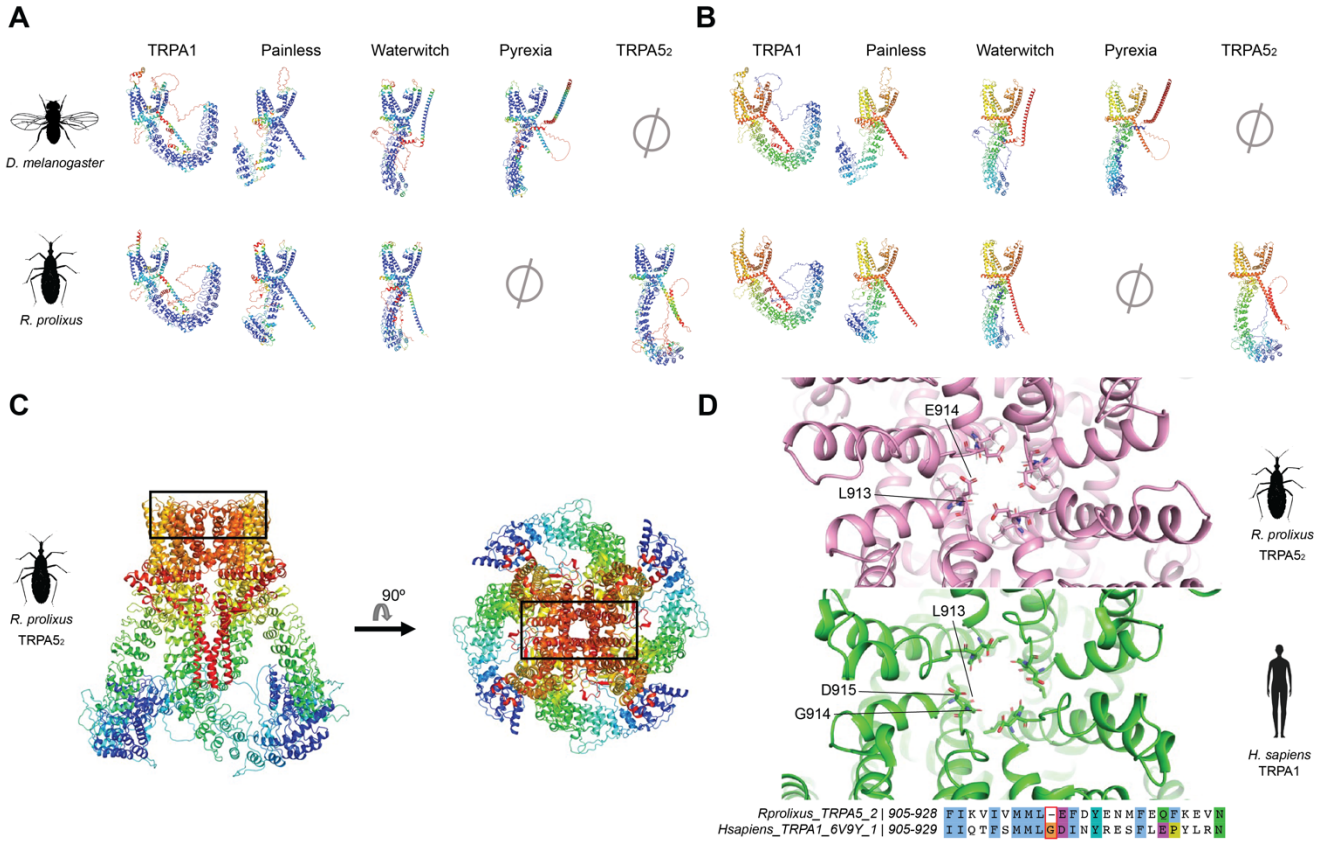

Figure 2. Predicted tetrameric structure of Rp-TRPA5$_2$ alongside monomers of all TRPA homologs in *Drosophila melanogaster* and *Rhodnius prolixus*. **A.** TRPA monomers colored by pLDDT score from the AlphaFold modeling. Blue represents a plDDT score of more than 90, reflecting a high confidence. **B.** TRPA monomers colored by chain bows, with the N-terminus in blue and the C-terminus in red. **C.** Tetrameric model of *R. prolixus* TRPA5$_2$, colored as chain bows as in B. The black box indicates the location of the selectivity filter shown in D. **D.** Top view of the selectivity filter of the pore of *R. prolixus* TRPA5$_2$ (top) and human TRPA1 (*H. sapiens*, pdb:6V9Y) (bottom). Three important residues identified by Zhao et al [56]– L913, G914 and D915 – are marked in TRPA1. The equivalent residues L913 and E914 are marked in TRPA5$_2$. The sequence alignment shows the selectivity filter. Note the glycine is absent in TRPA5$_2$ (see also Fig. S2).

Since dipteran and hemipteran insects lack *TRPA5* and *Pyrexia*, respectively, we asked if the two channels may occupy homologous structural and functional niches. From a pairwise overall comparison of the reliable monomeric models, despite the conserved regions mentioned above, Rp-TRPA5$_2$ appears to deviate from Dm-Pyrexia in three regions: the ARD, the transmembrane domain, and the pore helices that flank the selectivity filter (Fig. S4). First, Rp-TRPA5$_2$ possesses 14 AR

compared to 9 in Dm-Pyrexia, and displays longer loops, compared to Dm-Pyrexia and all other channels, including between the third and the fourth ankyrin repeats, within the fifth ankyrin repeat, and between the fifth and the sixth ankyrin repeats, counting from the N-terminus. This observation is interesting as ankyrin repeats are 31-33 residue protein motifs consisting of two α-helices connected by a ß-turn that occur in tandem arrangement to form ARDs critical for physiological processes [57], including a previously suggested role in thermal activation sensitivity [58, 59].

Hence, in vertebrates, two regions of 6 ARs each in the snake TRPA1 (AR3-8; AR10-15) have been shown to revert the channel thermal sensitivity by conferring heat-sensitivity to a chimeric AR human TRPA1 (Hs-TRPA1) [60]. Furthermore, transfer of a part of the ARD from Dm-TRPA1 (AR10-15), a region shown to control thermosensitivity in the fruitfly TRPA1, to Hs-TRPA1 also produced a heat-sensitive Hs-TRPA1 [60]. The temperature-dependent dynamics of the ARD has also recently been investigated in the TRPV1 channel, demonstrating that the ARD undergoes structural changes at similar temperatures that lead to TRPV1 activation, which suggested a potential role in the temperature-dependent structural changes leading to the channel opening [58]. The N-terminus region of mosquito TRPA1 also seems to be quite critical for heat-sensitivity [19]; however, there have been contradicting data for TRPA1, both from human and mosquito, arguing that additional regions controlling thermosensitivity are located outside the ARD [26, 61]. Another interesting feature is the disruption in the ankyrin repeat stacking between the fifth and the sixth ankyrin repeat in both Rhodnius and Drosophila Painless, which is not seen in Dm-Pyrexia and Rp-TRPA5$_2$. This breaking point coincides with the resolved N-terminal end of the recently reported structure of Dm-TRPA1-A in state 2, which is suggested to represent a temperature sensitized, pre-opened conformation of the channel [55]. Although additional functional evidence that ARDs may play a general role in insect TRP thermosensitivity is needed, these differences between Painless, Pyrexia and TRPA5 hint at a similar activation mechanism in Painless as proposed for TRPA1, yet potentially distinct from the activation mechanism of Dm-Pyrexia and Rp-TRPA5$_2$. In contrast, the shape of the ARD in Dm-Pyx, Dm-Wtrw

and Rp-Wtrw all exhibit remarkable similarities compared to that of Rp-TRPA5$_2$ (Fig. 2A) and the predicted number and position of ankyrin repeats also appears remarkably conserved between *R. prolixus* and *D. melanogaster* for TRPA1, Painless, and Wtrw (Table 2) suggestive of potentially conserved interspecific functions for each Rhodnius ortholog of the latter three channels.

Second, looking at the selectivity filter and the upper gate of the Rp-TRPA5$_2$ tetramer model (Fig. 2C and D), one conserved glycine (Gly914) is notoriously absent in Rp-TRPA5$_2$ (Fig 2D). This is striking as it is conserved in most other TRPAs, and either conserved or substituted for Serine or Threonine in most other non-hemipteran TRPA5 proteins (Fig. S2). Comparing it to a structure of Hs-TRPA1 published by Zhao et al. (PDB:6V9Y) [56], the Leu913 and Glu914 in Rp-TRPA5$_2$ seem to remain largely in the same locations as Leu913 and Asp915 in Hs-TRPA1, despite the shorter pore loop. The main difference therefore is that there are only two carbonyls in the pore loop of Rp-TRPA5$_2$, as opposed to three carbonyls in Hs-TRPA1. Although the difference is smaller than anticipated, since Gly914 is suggested to be important in gating, and lies in the location of the selectivity filter, this may affect permeation properties of Rp-TRPA5$_2$.

Finally, a difference in the lower gate can be seen where the Hs-TRPA1 structure is much narrower than that of Rp-TRPA5$_2$, and where the pore of the Rp-TRPA5$_2$ model is blocked by the position of the sidechain of Glu914. Since AlphaFold is better at modeling backbone folding than individual sidechains, the significance of this finding may be limited, but the Rp-TRPA5$_2$ model features a narrower pore than Hs-TRPA1 resolved in a closed conformation in complex with an antagonist [56].

Our findings that Rp-TRPA5$_2$ shares several conserved features of ankyrin TRPs, as well as unique structural novelties, raises the question as to whether Rp-TRPA5$_2$ may have undergone selection to fill the same function as *Pyrexia*, or whether its distinctive structural features may underlie a new type of thermosensitivity phenotype. If so, it would be interesting to determine whether the heat activation of the channel may be affected.

Table 2. Number of Ankyrin repeats observed in each monomer structure of thermos TRPA of *Rhodnius prolixus* and *Drosophila melanogaster.*

	Number of Ankyrin repeats	
Name	*Rhodnius prolixus*	*Drosophila melanogaster*
TRPA1	17	17
Painless	10	10
Waterwitch	9	10
Pyrexia		9
$TRPA5_2$	14	

TRPA5₂ encodes a novel class of thermosensitive insect receptor

In order to demonstrate a potential role of candidate $TRPA5_2$ as a thermosensitive ion channel, we optimized an *in vitro* cell-based platform to record temperature-elicited currents from HEK293T cells under whole-cell patch-clamp configuration. We transiently expressed a bicistronic T2A-fluorescent marker cassette [62] together with the candidate TRP channel, which localized well to the plasma membrane (Fig. S5). We delivered a fast heat stimulus by coupling an infrared laser diode fiber optic [63] to a PID controller that conveyed millisecond current pulses (Fig. S6).

At the molecular level, non-denaturing SDS-Page analysis showed that Rp-$TRPA5_2$ assembles similarly to other TRPs as a membrane-bound tetramer when expressed in HEK293T cells (Fig. S5). To validate the infrared (IR) patch clamp system, we first transiently expressed two known thermoTRPs, the rat TRPV1 (rTRPV1) and fruit fly TRPA1 isoform D (Dm-TRPA1-D) (Figs. S6, S7), both of which formed expected homotetrameric structures (Fig. S5). First, we used the ionic current increments through the open patch pipette (holding potential -2 mV), to calculate the temperature

changes associated with the different laser intensities. Typically, the current pulses were set to result in temperature increments at the cell membrane in the range of 23.5-71.7°C. A similar laser stimulation protocol led to marginal whole-cell current changes in non-transfected cells (Fig. 3A, Fig. S7A-B). Compared to non-transfected cells, we then observed a strong increase in the current amplitude of cells expressing rTRPV1 (Fig. 3B, Fig. S7C-D) with an enthalpy change associated with the activation of 88.3±9.4 kcal/mol, which is comparable to the published enthalpy values obtained using millisecond temperature jumps of ΔH = 85 kcal/mol, $T_{1/2}$ = 47.5°C for rTPRV1 (calculated from enthalpy and entropy values for steady-state activation from Yao et al. 2010, see Table 1) [63-65]. A temperature-induced activation response was also observed for the heat activated fruit fly channel, Dm-TRPA1-D, for which in our more precise setup, at 46.3°C [22], the open probability (Po) of the channel is about 10% (Po=0.1), corroborating a noxious activation temperature > 42°C [22]. Assuming complete activation by temperature of this channel (Po=1), which was not measured in previous studies due to limitations in the maximum temperature to which the Dm-TRPA1-D channel could be subjected, the activation process is characterized by an enthalpy change ΔH= 68.7±13.1 kcal/mol and $T_{1/2}$ = 53.5°C (Fig. 3C, Fig. S7E-F). These results demonstrate highly consistent biophysical properties of known thermoTRP channels evaluated with our laser-based delivery method, using the modified C-terminus in our expression cassette.

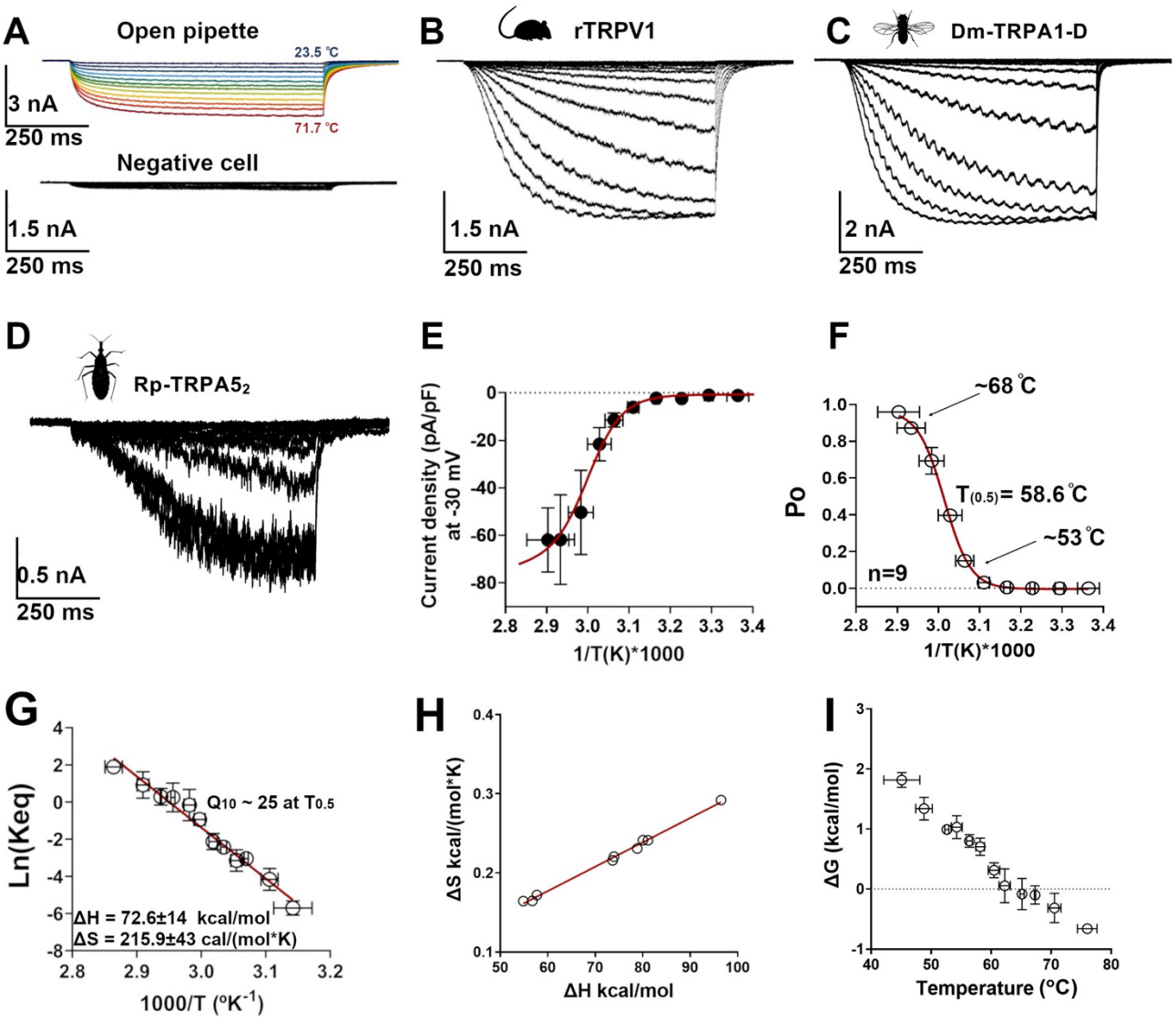

Figure 3. Thermodynamics of Rp-TRPA5$_2$ temperature-activated currents. A. Activation time course of temperature for the open pipette calibration (upper panel), and baseline current traces for a control cell (non-transfected). During each voltage pulse, a temperature step of 700ms was presented from room temperature to 71°C. **A.** Open patch-clamp pipette current traces in response to increasing voltage pulses (10 - 23 mV at 1 mV voltage inputs). **B.** Whole-cell currents evoked by temperature at -30mV of HEK293T cells expressing rat TRPV1, the heat-activated mammalian vanilloid thermo-TRP channel. **C.** Whole-cell currents evoked by HEK293T cells expressing Dm-TRPA1-D. **D**. Whole-cell currents evoked by HEK293T cells expressing Rp-TRPA5$_2$ under whole-cell configuration patch-clamp, held at -30 mV (n=9). Negative currents indicate that Rp-TRPA5$_2$ is a cationic channel. Data are presented as means ± standard errors. **E**. Current-Temperature relationship for Rp-TRPA5$_2$ where current density is plotted after normalization by cell membrane capacitance

and scaling to the mean maximum. **F.** Fraction of Rp-TRPA5$_2$ channels in the open state (Open probability, P_o) as a function of the temperature. The Po vs 1/T was fitted to a Boltzman function with the midpoint of activation ($T_{1/2}$) reached at 58.6 °C. **G** Van't Hoff plot estimates of Rp-TRPA5$_2$ with an activation enthalpy of the endothermic transition at 92 kcal/mol and an entropic change associated to the temperature activation process at 274 cal/mol*K. at -30 mV as a function of the temperature [63]. **H**. Coupling between enthalpic (ΔH) and entropic (ΔS) changes for each one of the experiments recorded **I**. ΔG vs. temperature plot for Rp-TRP5A$_2$ channels, temperature activation is associated with small ΔG (free energy) changes, as reported for other families of mammalian thermo receptors. ΔG was calculated as -RT*ln(Keq) [66].

Finally, when holding the membrane potential at -30mV in patched mRuby2-expressing cells transfected with Rp-TRPA5$_2$, whole cell currents were evoked by temperature steps from 53°C to 68°C (Fig. 3D, 3E). The average temperature for the activation "threshold" was 53°C, defined as Po = 0.1 calculated from the Van't Hoff plots. The channel opening appeared to saturate at 68°C (Po=0.9) (Fig. 3F), with a $T_{1/2}$ = 58.6°C. The steady-state parameters of activation were calculated from the current at the end of the 700 ms temperature pulse. The current density versus temperature relationship (Fig. 3E) indicates that the opening of Rp-TRPA5$_2$ involves an activation enthalpy of approximately 72.6±14 kcal/mol (Fig. 3G). Similar large enthalpy changes ranging from 60 to 200 kcal/mol are involved in the opening of TRPM8, TRPV1, and TRPV2 [9], supporting that the TRPA5 ion channel activity is extremely temperature-dependent with high enthalpy change associated with the channel opening. The large entropy value further indicates that the channel transits between a highly ordered closed state and a strongly disordered open configuration, similarly to TRPV1 (316 cal/mol·K at -60mV). Altogether, these results demonstrate that Rp-TRPA5$_2$ acts as an insect thermoTRP receptor of noxious heat *in vitro*.

Based on the open probability (Po), we calculated a Q_{10} value of ~ 25, which is in the range of characterized noxious vertebrate (rTRPV1 Q_{10} = 16.8; rTRPV2 Q_{10} = 20.6) and invertebrate thermoTRPs (fruit fly Pyrexia Q_{10} = 18.2) (Table 1). From a thermodynamic point of view, many TRP ion channels are modulated by temperature [67], but our results clearly support that TRPA5$_2$ belongs to a restricted category of thermoTRPs as it is directly activated by temperature as the sole stimulus

[8, 66]. Rp-TRPA5$_2$ appears to be activated in a higher noxious range compared to all known invertebrate thermoTRPs thus far (Fig. 1A, Table 1, Fig. S2) including the fruit fly Painless and TRPA1 channels that mediate thermal nociceptive escape through larval mdIV neurons at temperatures above 40°C and 46°C, respectively [17], or Pyrexia channels that induce paralysis in adult flies upon exposure to 40°C [18]. In mammals, only TRPV2 contributes to highly noxious (>52 °C) heat sensing [64, 68, 69].

ThermoTRP channels can integrate voltage and temperature allosterically [67]. We aimed to establish the temperature sensitivity of the channel directly from the Van't Hoff plot, and not from the influence of temperature on the voltage activation process, allowing us to establish the thermodynamics of temperature activation process independently from other stimuli. Using fast temperature jumps, we could activate Rp-TRPA52 channels directly, validating that the channel is a thermoTRP in the noxious temperature range. In addition, similarly to rTRPV1 and Dm-TRPA1-D, Rp-TRPA5$_2$ has large enthalpy changes related to the channel activation, which is related to the high sensitivity of these channels to temperature changes. In rTRPV1, thermal activation at +60 mV causes only a relatively small enthalpy change (30 kcal/mol) compared to 100 kcal/mol when rTRPV1 is activated at -60 mV, representing a three-time increase in temperature sensitivity at negative voltages [63]. Similarly to rTRPV1, Rp-TRPA5$_2$ shows almost no heat-elicited activity at depolarized potentials (> 0mV), but a robust response at negative voltages (-30mV). Although the temperature activation for Rp-TRPA5$_2$ appears very similar to Dm-TRPA1-D and rTRPV1, the activation kinetics of Rp-TRPA5$_2$ is slower compared with these channels, which could be due to intrinsic molecular interactions influencing the transition between closed and open states [67], in light of our observations of several key defining structural differences. This difference in the opening kinetics has been observed before for other thermoTRPs, like the temperature-dependent HsTRPV3, which exhibits a high temperature sensitivity, comparable to hTRPV1, but presents slower kinetics [65, 70].

TRPA5's physiological role as a noxious heat sensor

Sensory receptors in the same clades are often tuned to detect a stimulus over a discrete window of intensities, enabling the recognition of physiologically relevant cues over a wide dynamic range [1, 3, 71]. The TRP Ankyrin family is an excellent example of this pattern, as distinct, yet closely related channels account for thermal responsiveness over a range from innocuous to noxious heat [4, 12]. In addition, orthologous thermoTRPs often have different activation temperatures, and this has been postulated to reflect functional adaptive evolution to different optimal temperatures, coordinating thermoregulatory behaviors such as host seeking, thermal avoidance, and tracking of optimal temperatures [72]. Our findings on the temperature activation of Rp-TRPA5$_2$, a TRPA clade not functionally characterized, clearly support a role for this previously orphan gene as a molecular sensor in the noxious heat spectrum. Notably, a known noxious heat receptor in Diptera, *Pyrexia,* is missing from *Rhodnius*, while a TRPA5 ortholog has not been found in flies and mosquitoes*,* raising the interesting possibility that convergence and functional redundancy might account for the evolutionary patterns of differential gain and retention of thermoTRPs in insects.

Consistent with a role as a noxious thermosensor, quantitative analyses show that Rp-TRPA5$_2$ is expressed broadly across tissues, with high levels detected in the head, rostrum, legs, thorax, abdomen and to a lesser extent in the antennae (Fig. 1, Fig. S3). By qPCR, we detected the highest expression in the head (Fig. S3), in agreement with previous transcriptomic analyses [37] and remarkably similar to the expression pattern of *Pyrexia* in the fruit fly [18]. Noxious environmental temperatures are extremely common in natural environments of small insects with low thermal capacity, thus, detecting and avoiding heat is critical to prevent injury. Temperature distributions vary widely for natural objects. For instance, dry and moderately gray-colored or dark objects such as tree bark or rocks easily reach temperatures above 50°C [73]. If the humidity level is high, and radiative cooling of the sky is not effective, the same objects can reach temperatures above 60°C in the full sun. For example, temperatures of dry leaf substrates on the ground can exceed 50°C in full sun since they do not undergo evaporative cooling, which would typically prevent a leaf's surface temperature from going above 40°C. In lab simulated natural environments and in field thermal imaging studies,

insects can reach 60°C under full sun with high humidity in as little as 15 seconds [73]. Considering that Rhodnius adults are about 3 cm in length and dark colored, with a small thermal capacity, and that they typically inhabit tropical environments with high humidity, they are likely to rapidly reach temperatures above 60°C if exposed to full sun, suggesting that TRPA5 may mediate noxious heat avoidance. Although the physiological and behavioral role of Rp-TRPA5$_2$ will need to be examined in detail, the discovery of the activation range of TRPA5$_2$, opens avenues for exploring the convergent evolution of noxious heat sensing between TRPA5$_2$ in Rhodnius bugs and *Pyrexia* in Drosophila flies, and for assessing whether it is also relevant for both inner temperature regulation and warm substrate avoidance.

To better understand the mechanisms of Rp-TRPA5$_2$ function and heat stimulus integration, future studies could examine co-expression with other TRPs. Rp-TRPA5$_2$ is also expressed in antennae, albeit at lower levels (Fig. S3). Antennae in triatomine bugs function as a multimodal sensory organ, notably harboring highly specialized thermosensory sensilla involved in the detection of host signals such as heat and moisture [36]. Heat sensing in triatomines is driven by air temperature gradients around the host (conductive heat) [39, 40] as well as infrared radiation [74]. Antennal thermoreceptors are known to be required for orientation and distance estimation [75] as well as for precisely locating warm skin blood vessels before initiating proboscis extension and biting [76]. Similarly to homologous noxious heat detectors in mosquito antennae, Rp-TRPA5$_2$, might contribute to tuning host-selective thermotaxis to avoid stimuli exceeding host temperatures. An interesting next step would be to map the cellular location of Rp-TRPA5$_2$ in peripheral sensory neurons to investigate potential colocalization with other channels involved in innocuous heat detection.

372 **TRPA5 as novel target to mitigate the impact *Rhodnius prolixus* in the transmission of Chagas**
373 **disease**

374 ThermoTRPs are polymodal sensors of physical and chemical stimuli [71]. For example, channels in
375 the insect TRPA1 and HsTRPA clades are typically activated by AITC and various plant-derived
376 chemicals such as carvacrol and citronellal [23, 28, 29]. However, characterized receptors of noxious
377 heat in insects such as Pyrexia and Painless do not exhibit chemical sensitivity to electrophiles [17].
378 Since our phylogenetic analyses support that Rp-TRPA5$_2$ is the sister clade to TRPA1, it is possible
379 that Rp-TRPA5$_2$ also plays a chemosensory role. Indeed, live Rhodnius treated with capsaicin, the
380 vanilloid pungent extract of chili peppers, were recently shown to have impaired orientation towards a
381 thermal source [77]. Notably, this compound can directly activate the mammalian TRPV1 receptor
382 independent of temperature, and the mammalian noxious temperature receptor, TRPV2, when bearing
383 only four mutations [3, 15]. Other than capsaicin, both TRPV1 and TRPV2 are readily activated by
384 additional vanilloid compounds such as resiniferatoxin, an active compound from the cactus *Euphorbia*
385 *resinifera* used for medicinal purposes and other plant-derived compounds that act as chemical
386 agonists [78]. Findings of botanical compounds triggering chemical activation of TRPA5$_2$ combined
387 with *in vivo* behavioral exposure studies, may thus contribute to uncovering new classes of natural
388 repellents potentially co-mediating heat-avoidance. This would be significant, not only in Rhodnius but
389 also for other triatomines and hemipteran vectors sharing a close TRPA5$_2$ orthologue such as the bed
390 bug, *Cimex lectularius*. Together, our study deorphanizes and characterizes the first ankyrin TRPA5
391 ion channel acting as noxious heat sensor, consistent with independent evolutionary origins of the
392 molecular transduction of noxious stimuli in insects, while simultaneously opening the door for further
393 pharmacological studies of TRP receptors in triatomine vectors.

Material and Methods

Phylogenetic analyses. Amino acid sequences of insect TRPA channels from the Anoplura (sometimes included under Psocodea or Phthiraptera), Coleoptera, Diptera, Hemiptera, Hymenoptera, Isoptera and Lepidoptera insect orders were retrieved from the InsectBase repository [79], FlyBase version FB2020_03 [80], VectorBase (https://www.vectorbase.org), BeeBase [81], NCBI-blast [82], EnsemblMetazoa (https://metazoa.ensembl.org), the i5k Workspace@ NAL [83] and OrthoFinder [84]. The TRP sequences from insect model systems including *Drosophila melanogaster*, *Tribolium castaneum*, *Bombyx mori*, *Apis mellifera* and *Rhodnius prolixus* were used as templates to mine and curate orthologous TRP ORF sequences from annotated insect genomes and transcriptomes. To classify the uncharacterized TRPs, amino acid sequences were aligned using MAFFT [85], and Maximum-Likelihood phylogenetic trees were inferred in IQ-TREE v1.6.11 using ModelFinder (Ultrafast Bootstrap, 1000 replicates), using a best-fit model JTT+F+I+G4 measured by the Bayesian information criterion (BIC) [86-88]. The phylogenetic trees were visualized, rooted at mid-point and annotated in R V3.6.3 using the ggtree package [89] and Evolview [90]. The accession numbers are listed in Table S1.

TRPA5 gene annotation and tissue expression. We collected Illumina read data from *R. prolixus* tissue libraries published in the Sequence Read Archive (SRA) at NCBI under Bioproject accession numbers PRJNA281760/SRA:SRP057515 (antennal library from larvae, female adult and male adult), PRJEB13049/SRA:ERP014587 (head library), and PRJNA191820/SRA:SRP006783 (ovary and testes library). We performed low-quality base trimming and adaptor removal using cutadapt version 1.16 [91] and aligned the trimmed read pairs against the *R. prolixus* assembly version RproC3.0.3 (retrieved from VectorBase.org) genome using HISAT2 version 2.2.0 [92]. The existing annotation was used to create a list of known splice sites using a python script distributed with HISAT2. We used StringTie version 2.1.3b [93] with the *conservative* transcript assembly setting to improve the annotation, reconstruct a non-redundant set of transcripts observed in any of the RNA-Seq samples, and compute expression estimates.

We applied Trinotate version 3.2.1 [94] to generate a functional annotation of the transcriptome data. In particular, the functional annotation of TRP genes for which the initial genome annotation was absent or incomplete (i.e *TRPA5, Nan, Pain*) were localized in Trinotate annotation followed by validation using the Apollo

gene browser [95]. Rp-TRPA5-A, Rp-TRPA5-B and Rp-TRPA5-C are three independent loci. Therefore, we opted to rename them *Rp-TRPA5*$_1$, *Rp-TRPA5*$_2$, and *Rp-TRPA5*$_3$, respectively, to avoid confusion with standard gene isoform nomenclature, which applies in the case of TRPA1-A and TRPA1-B, two isoforms of the Rhodnius *TRPA1* locus. All TRP gene identifiers are presented in Table S2.

The alignment BAM files were used to estimate transcript abundance using StringTie together with our improved annotation. The abundance tables from StringTie were imported into R using the *tximport* package [96], which was used to compute gene-level abundance estimates reported as FPKM. We used the R package *pheatmap* to visualize the expression level of TRP genes.

Monitoring of TRPA5$_2$ expression levels by quantitative PCR. Live adults of *R. prolixus* were obtained from BEI Resources (USA). Female antennae, rostrum, legs, heads (minus antenna and rostrum), and bodies (thorax minus legs + abdomen) were dissected and pooled from 15 individuals in DNA/RNA shield reagent (Zymo) and stored at -20°C until further processing. Total RNA was isolated using the Monarch RNA extraction procedure (New England Biolabs), including tissue grinding in liquid nitrogen and a DNAse I step. cDNAs were synthesized using the GoScript cDNA synthesis procedure (Promega) prior to concentration assessment using the Qubit High sensitivity DNA kit (Invitrogen). Two gene-specific primer (GSP) sets were designed for Rhodnius Actin (Genbank acc. Nr. EU233794.1) and TRPA5$_2$ using Primer3 version 2.3.7 in Geneious [97] (Table S3). Each primer set was initially validated by calculating standard curves from serial dilutions of template cDNA (2 ng/µL to 0.25 ng/µL) and primer mix (5 to 0.25 µM) with choosing amplification efficiencies (E) between 95 and 100%. qPCR amplification products from initial runs were additionally checked on 2% agarose gels to verify the correct amplicon sizes and the absence of primer dimers. As a final validation, qPCR products were purified using Exo-SAP (Fermentas) prior to Sanger sequencing to ensure product amplification specificity. Quantitative PCR reactions were then run in three technical replicates on a CFX384 Real-Time PCR system (Bio-Rad) with quantification and dissociation curves analyses performed for three independent experiments using the CFX Maestro Software 2.3 (Bio-Rad). Each five-microliter reaction contained 2.5 µL 2x SsoAdvanced Universal SYBR Green Supermix (Biorad), 0.25 ng cDNA and 0.125 µM primers. Cycling conditions were as follows: 95°C for 2 min, 39 cycles of 95°C for 10 s, 60°C for 10 s followed by a dissociation curve analysis from 65.5°C to 89.5°C with gradual heating at 0.6°C/s. Relative log-fold expression levels were normalized per tissue type against the reference gene and calibrated relative to Antennae (log fold expression = 1).

Alpha-fold modeling and DALI analyses. Monomer structures of Rhodnius TRPA1, Rhodnius Painless, Rhodnius Waterwitch, Rhodnius TRPA5$_2$, Drosophila TRPA1, Drosophila Painless, Drosophila Waterwitch and Drosophila Pyrexia were generated using AlphaFold2 with amber relaxation activated [51] on Colab's server [53]. To model the Rhodnius TRPA5$_2$ tetramer, due to limitations in computational power, the transmembrane region (residues 608-1078) was modeled first, and then used as a custom template to model a monomer of residues 42-1078. The first 41 residues and the C-terminal of the monomers from residue 1079 were disordered and truncated to avoid clashes when assembling the tetramer. A tetramer was assembled of four copies of the monomer by aligning them to each of the chains of the truncated transmembrane tetramer in PyMOL [98]. The monomer models were compared with pairwise structural alignment using the Dali server [99]. The PDB files are provided as supplementary material.

Molecular cloning. Antennae from twenty Rhodnius adult individuals were obtained from a laboratory culture (Orchard lab, University of Toronto Mississauga, Canada) and stored in DNA/RNA Shield™ reagent (Zymo Research). Tissues were disrupted in Trizol using a Premium Multi-Gen 7XL Homogenizer (PRO Scientific) and RNA was subsequently extracted using the Direct-zol RNA kit (Zymo Research), including a DNAse step to remove genomic DNA contamination. cDNA was synthesized from 1ug Total RNA using the GoScript™ Reverse Transcriptase kit (Promega) and random hexamers following the recommended manufacturers' protocol. RNA and cDNA qualities were verified using a Nanodrop (Nanodrop 2000/2000c UV-vis spectrophotometer, Thermo Scientific) and quantified using a Qubit Fluorometer (ThermoFisher). The coding regions of Rhodnius *Rp-TRPA5$_2$* was amplified from antennal cDNA using gene-specific primers designed based on Rhodnius full length TRP sequences [37] and containing unique restriction sites (Table S3). PCR reactions were performed in a Veriti™ Thermal Cycler (ThermoFisher) using the Advantage® 2 PCR Kit (Takara Bio) in a touchdown cycling program as follows: 95°C for 2 min, 16 cycles of 95°C for 30 sec, 68°C for 1 min (-0.5°C/cycle), 68°C for 4 min followed by 20 cycles of 95°C for 30 sec, 60°C for 1 min, 68°C for 4 min, and a final step at 68°C for 10 min. Amplification products were analyzed by electrophoresis, and fragments of expected size were excised from the gel, purified using the Monarch® DNA gel extraction kit (NEB) and subjected to Sanger Sequencing for ORF sequence-verification prior to codon-optimization at Genscript and subcloning. For the rat rTRPV1 and the fruit fly Dm-TRPA1-D, gene specific primers (Table S3) were used to amplify the ORF including suitable flanking restriction sites prior to gel purification and double restriction digestion. The digested PCR products were gel

purified and ligated in an expression cassette containing the human cytomegalovirus (CMV) immediate early promoter and engineered to include a C-terminal tag by the monoclonal antibody FLAG epitope sequence (DYKDDDDK), followed by a Ser-Gly-Ser linker peptide, a T2A peptide sequence (EGRGSLLTCGDVEENPG) and the coding region of the cytoplasmic fluorescent marker protein mRuby2 [62, 100]. The ligation mixtures were used to transform *Stbl3* competent *E. coli* cells (ThermoFisher) using standard protocols. Plasmid DNAs were purified using the Qiaprep spin Miniprep (Qiagen) and verified by Sanger sequencing using internal gene-specific and vector primers to ensure overlapping sequence information in both forward and reverse directions. High yield pure plasmid DNA preparations were subsequently obtained from 100 mL overnight LB broth cultures using the endo-free ZymoPURE™ II Plasmid Midiprep Kit (Zymo Research, USA).

Transient HEK293T cell expression. Plasmid DNAs clones from TRP cDNAs were transiently expressed in HEK293T cells to optimize expression conditions via mRuby2 visualization and western blot analysis prior to whole cell patch clamp recordings. HEK293T cells were seeded at a density of 0.6 x 10^6 cells on day 0 in 60 mm culture dishes (ref 25382-100, VWR) in DMEM High Glucose, GlutaMAX (Life Technologies) supplemented with 10% FBS (Seradigm Premium, VWR, USA). For each transfection, lipid complexes containing 2.5 µg DNA: 10 µL L2000 (Life Technologies) mixed in Opti-MEM I Reduced Serum (Life Technologies) were added dropwise to the cells at 50% confluency (1.2 x 10^6 cells, day 1). The culture medium was exchanged with new DMEM/FBS medium six-hours post-transfection. Cells were incubated at 37°C in a humidified HERAcell 150i incubator (Thermo Scientific) with 5% CO_2.

Biochemistry. For whole-cell TRP expression analysis, cells were harvested 72h post-transfection; the medium was decanted, cells were collected in 2mL cold D-PBS, centrifuged for 5 min at 4,000 rpm at 4°C and then the supernatant was discarded. The cell pellet was gently suspended in 50 µL cold Ripa lysis buffer (Thermo Scientific) supplemented with 1% Triton-X100 (Sigma-Aldrich) and complete EDTA-free protein inhibitors (Sigma-Aldrich). Cell membranes were lysed for 1h at 4°C with gentle rotation on a sample homogenizer, and cell debris were collected by centrifugation at 4°C for 15 min at 13,000 rpm. The crude protein lysate concentration was quantified by bovine serum albumin (BSA) (Sigma-Aldrich) and 25 µg crude extract was loaded on NuPAGE™ 3-8% Tris-Acetate gels (ThermoFisher) and transferred to a polyvinylidene difluoride membrane on a TurboBlotTransfer system (Bio-Rad Laboratories). The membranes were blocked with 5% milk (Bio-Rad) in Tris-buffered saline containing 0.1% Tween 20 (TBST, Bio-Rad) and incubated overnight with aFLAG antibody 1:2,500 (GE Healthcare) on a gently rocking platform at 4°C. After washing with TBST the

membranes were incubated for 1h at ambient temperature in the dark with horseradish peroxidase (HRP) ECL anti-mouse conjugated antibody (Amersham, USA) diluted in 5% milk in TBS-Tween at 1:2,500. Membranes were rinsed in TBST and revealed using the SuperSignal West Femto (Thermo Scientific) and imaged on a ChemiDoc system (Bio-Rad Laboratories).

For membrane surface expression, the plasma membrane expression of Rp-TRPA5$_2$ channels was assessed using the Pierce Cell surface Protein isolation kit (Thermo Scientific). On day 0, four T75 cm^2 flasks were seeded with 1 x 10^6 HEK293T cells. Forty hours later, each flask was transfected with lipid complexes containing 48 µg endo-free plasmid DNA and 96 µl Lipofectamine 2000 diluted in Opti-MEM serum and incubated at 37°C. 72 hours post-transfection, cells were gently washed with ice-cold PBS, labeled with Sulfo-NHS-SS-Biotin, and harvested following the manufacturer's protocol. Cells were lysed on ice for 30 min in the manufacturer's lysis buffer supplemented with 0.5% Triton-X100 and complete EDTA-free protein inhibitors (Sigma-Aldrich), with gentle 5s vortexing every 5 min, and two 5x-1s sonicating bursts on ice. Following centrifugation, the cell lysate was bound to NeutrAvidin agarose resin and gently mixed for 60 min at ambient temperature on a platform rotator. The membrane-bound fraction was eluted with 50mM Dithiothreitol in SDS-Sample buffer (62.5 mM Tris/HCl pH6.8, 1% SDS, 10% Glycerol) and then placed on ice. For Western Blot analysis, 32 µl of the membrane protein eluate fraction were mixed with Laemmli buffer (Bio-Rad) supplemented with 10% 2-mercaptoethanol. Sixteen µl of the homogenized protein-loading buffer sample were loaded in duplicates on a NuPAGE™ 3-8% Tris-Acetate gel (ThermoFisher) to be probed separately with FLAG and ATPase antibodies. Proteins were separated by electrophoresis for 3h at 80V at 4°C, then transferred to a polyvinylidene difluoride membrane on a TurboBlotTransfer system (Bio-Rad Laboratories). The membranes were blocked in parallel with 5% milk (Bio-Rad) in Tris-buffered saline containing 0.1% Tween 20 (TBS-T, Bio-Rad) and incubated overnight on a gently rocking platform at 4°C with aFLAG antibody 1:2,500 (GE Healthcare) or with Anti-Sodium Potassium ATPase antibody 1:2,500 (ab76020, Abcam) diluted in 5% milk. After three washes with TBST, the membranes were incubated for 1h at ambient temperature in the dark with HRP ECL anti-mouse conjugated antibody (Amersham, USA) at a 1:2,500 dilution in 5% milk/TBST. Membranes were rinsed in TBST and revealed using the SuperSignal West Femto (Thermo Scientific) and imaged on a ChemiDoc system (Bio-Rad Laboratories).

Temperature control using a laser system. We used a manual patch-clamp station (Axopatch 200, Molecular Devices) equipped with a fiber-delivered laser system to record temperature-activated currents under a precise voltage-clamp control. The setup was modified after Yao et al (2009) [101] (Fig. S5) and takes advantage of water's IR absorption band to generate rapid temperature jumps from RT to high temperatures. It combines an infrared diode laser (λc =1460 nm (+/-20 nm), Output power = 4.8 watts) (Seminex Inc.) coupled with a 100-um optical fiber with a striped tip (ThorLabs, Inc.) as the controllable heat source. Two independent micromanipulators allowed us to precisely align the relative positions of the patch-clamp electrode and the fiber on a single cell (Fig. S8). To calibrate the optic fiber position with respect to the patch pipette we used a visible laser (Fig. S8). Marks on the computer screen were used to keep the position of the fiber and the pipette consistent for the different experiments. Cells under whole-cell voltage-clamp control were held at -30mV during the experiment. To program fast pseudo-transient temperature changes, the patch pipette current was used to read the temperature changes in real-time as the feedback to the laser diode controller (LDC-37620, ILX Lightwave) to perform proportional-integral-derivative (PID) control of the driving current of the laser diode (*see Extended Methods*). This laser-heating setup provides a rapid and precise heating rate on the order of 50°C within tens of milliseconds, essential to provide both adequate temporal resolution and controllable steady-state temperatures in the range of 35°C to 70°C to analyze the channel activation. Fig. S7A shows constant temperature steps were achieved with a rising time constant of 34.2±3.3 ms, independent of the laser power. The temperature jump associated with successive current pulses is precisely calculated by running an open pipette calibration following the same current sequence at the end of each run (Fig. S6).

Temperature calibration. We used the resistance of the open pipette to measure the temperature jump magnitudes following the equation $T=\{1/T_0 - R/E_a \times \ln(I/I_0)\} - 1$, where R is the gas constant, T_0 and I_0 are respectively room temperature and the corresponding electrode current at room temperature. The activation energy (E_a) of the system corresponds to 3.84 kcal/mol as was established by Yao et al. (2009) for the pair of solutions used in the recordings [101]. The equation describes the change in ion motility as a function of temperature changes in the system. The current change was used as a feedback signal for a laser-diode controller software coded in Labview that uses a proportional-integral-derivative (PID) control algorithm. To account for the variability in the diameter between the different patch pipettes used in different experiments, the instrument was calibrated before each experiment to assure comparable temperature jumps in each experiment, adjusting the diode power outputs to the desired temperature accordingly.

Whole cell patch-clamp recordings. Cells were seeded at low density in a 30 mm culture dish (VWR) containing round glass coverslips 48h post-transfection (Table S5, Fig. S5). Cells were first rinsed with D-PBS at room temperature, trypsinized with 0.5 mL Accutase (Stemcell Technologies) and suspended in 4.5 mL pre-warmed DMEM-FBS medium. Two hundred microliters of this cell suspension were mixed with 1.8 mL pre-warmed DMEM-FBS medium, dispensed drop wise in the culture dish, and incubated for 24h at 30°C. In a typical experiment, one glass cover slip was gently retrieved from the culture dish using sterile forceps, rinsed with a recording solution using a Pasteur pipette and placed in the recording chamber (Fig. S6). The fluorescence of mRuby-expressing cells was monitored to select bright, healthy, isolated cells for whole-cell patch clamping. Experiments under the whole-cell configuration were carried out 72h after induction. The electrodes were fabricated with borosilicate capillaries, using a horizontal micropipette puller P-1000 (Sutter Instrument, Novato, CA, USA), and polished using a microforge (Narishige, Japan) to a final diameter between 2-4 um. The internal electrode was filled with the following solution in mM: 126 CsCl, 10 EGTA, 10 HEPES, 1 EDTA, and 4 MgATP. The extracellular recording solution contained 2 mM $CaCl_2$, 10 mM HEPES, 140 mM NaCl, pH 7.2 (adjusted with NaOH). The electrode resistance ranged between 2-4 MΩ, and the Vjp was estimated at ~18 mV for the recordings. The current traces were amplified using a MultiClamp 700B amplifier (Molecular Devices, Sunnyvale, CA, USA). The amplified electrical signals were acquired with a Digidata 1440A using the pClamp10 software (Molecular Devices, Sunnyvale, CA, USA). Series Resistance (Rs) was compensated in 80%, as well as the fast and slow capacitive components of the current. The current density was fitted to the following Boltzmann function:

$$I\_total = I\_leak\, e^{(-(\Delta H\_leak)/RT)} + (I\_max\, e^{(-(\Delta H\_i)/RT))}/(1 + e^{(-(\Delta G\_T)/RT)})$$

Whereby the first term ΔH_leak is the enthalpy change of the leak current. The second term accounts for the channel activity, with $\Delta G = \Delta H - T\Delta S$ is the free energy change involved in the closed-open reaction, and ΔH_i accounts for the linear temperature dependence of the ionic conductivity and leakage current [101]. The corrected temperature current density (*I*) was used to calculate the equilibrium constant from the relative fraction of the channel in the open conformation (Po), assuming a two-state model, where Po = I/Imax.

$$Po = 1/(1 + Keq^{-1})$$

where $\ln(K_{eq}) = -(\Delta H/RT) + (\Delta S/R)$. Thus from the Van't Hoff plots ln(Keq) vs 1/T, the enthalpy and entropy associated with the channel opening can be obtained [66].

Funding

This work was supported by a Mind Brain Behavior Interfaculty grant to NEP and MAL, an Alice and Knut Wallenberg fellowship at the Broad Institute of MIT and Harvard to MAL, National Science Foundation PHY-1411123 and PHY-1411445 to NEP and NY respectively, funding from Formas 2017-01463 to UJ and from the Carl Tryggers Foundation (CTS 21:1309) to MAL. The funders had no role in study design, data collection and analysis, decision to publish, or preparation of the manuscript.

Acknowledgments

The authors acknowledge Andrew Allen for helpful discussions on TRP biochemistry, Xi-Shi for early advice with HEK cell culture, Rhiannon Macrae for her valuable guidance, Feng Zhang for his support and for giving access to resources at the Broad, Ian Orchard for providing *Rhodnius prolixus* antennae, BEI resources (http://www.beiresources.org/) and Ellen M. Dotson for providing Rhodnius adults, Rachel Gaudet for providing a rTRPV1 plasmid template and Pengyu Gu for providing a Drosophila Dm-TRPA1-D (A10a, flybase PG) plasmid template.

Data Availability Statement

All datasets generated and analyzed for this study will be published as supplementary files accompanying the paper.

606 **References**

607 [1] McKemy DD. 2007 Temperature sensing across species. *Pflugers Archiv : European journal of*
608 *physiology* **454**, 777-791. (10.1007/s00424-006-0199-6).

609 [2] Vriens J, Nilius B, Voets T. 2014 Peripheral thermosensation in mammals. *Nature Reviews*
610 *Neuroscience* **15**, 573-589. (10.1038/nrn3784).

611 [3] Xiao R, XU S. 2021 Temperature sensation: from molecular themosensors to neural circuits and
612 coding principles. *Annual review of physiology* **83**, 205-230.

613 [4] Castillo K, Diaz-Franulic I, Canan J, Gonzalez-Nilo F, Latorre R. 2018 Thermally activated TRP
614 channels: molecular sensors for temperature detection. *Physical Biology* **15**, 021001.
615 (10.1088/1478-3975/aa9a6f).

616 [5] Garrity P, Goodman M, Samuel AD, Sengupta P. 2010 Running hot and cold: behavioral
617 strategies, neural circuits, and the molecular machinery for thermotaxis in *C. elegans* and
618 *Drosophila*. *Genes and Development* **24**, 2365-2382.

619 [6] Klein M, Afonso B, Vonner AJ, Hernandez-Nunez L, Berck M, Tabone CJ, Kane EA, Pieribone
620 VA, Nitabach MN, Cardona A, et al. 2015 Sensory determinants of behavioral dynamics in
621 Drosophila thermotaxis. *Proceedings of the National Academy of Sciences* **112**, E220-E229.

622 [7] Clapham DE. 2003 TRP channels as cellular sensors. *Nature* **426**, 517-524.
623 (10.1038/nature02196).

624 [8] Venkatachalam K, Montell C. 2007 TRP channels. *Annu Rev Biochem* **76**, 387-417.
625 (10.1146/annurev.biochem.75.103004.142819).

626 [9] Baez-Nieto D, Castillo J, Dragicevic C, Alvarez O, Latorre R. Thermo-TRP channels: biophysics
627 of polymodal receptors.

628 [10] Fowler M, Montell C. 2013 Drosophila TRP channels and animal behavior. *Life Sci* **92**, 394-403.

629 [11] Peng G, Shi X, Kadowaki T. 2015 Evolution of TRP channels inferred by their classification in
630 diverse animal species. *Molecular Phylogenetics and Evolution* **84**, 145-157.
631 (doi.org/10.1016/j.ympev.2014.06.016).

632 [12] Matsuura H, Sokabe T, Kohno K, Tominaga M, Kadowaki T. 2009 Evolutionary conservation
633 and changes in insect TRP channels. *BMC Evolutionary Biology* **9**, 228. (10.1186/1471-2148-9-228).

634 [13] Caterina MJ, Schumacher MA, Tominaga M, Rosen TA, Levine JD, Julius D. 1997 The
635 capsaicin receptor: a heat-activated ion channel in the pain pathway. *Nature* **389**, 816-824.
636 (10.1038/39807).

637 [14] Gracheva EO, JF C-M, Carcacia-González JA, Ingolia N, Manno C, Aranguren C, Weissman J,
638 Julius D. 2011 Ganglion-specific splicing of TRPV1 underlies infrared sensation in vampire bats.

639 [15] Caterina MJ, Rosen TA, Tominaga M, Brake AJ, Julius D. 1999 A capsaicin-receptor
640 homologue with a high threshold for noxious heat. *Nature* **398**, 436-441. (10.1038/18906).

641 [16] Vriens J, Owsianik G, Hofmann T, Philipp Stephan E, Stab J, Chen X, Benoit M, Xue F,
642 Janssens A, Kerselaers S, et al. 2011 TRPM3 Is a Nociceptor Channel Involved in the Detection of
643 Noxious Heat. *Neuron* **70**, 482-494. (doi.org/10.1016/j.neuron.2011.02.051).

644 [17] Tracey WD, Wilson RI, Laurent G, Benzer S. 2003 painless, a Drosophila Gene Essential for
645 Nociception. *Cell* **113**, 261-273. (10.1016/S0092-8674(03)00272-1).

646 [18] Lee Y, Lee Y, Lee J, Bang S, Hyun S, Kang J, Hong S-T, Bae E, Kaang B-K, Kim J. 2005
647 Pyrexia is a new thermal transient receptor potential channel endowing tolerance to high
648 temperatures in Drosophila melanogaster. *Nature Genetics* **37**, 305. (10.1038/ng1513).

649 [19] Kang K, Panzano V, Chang E, Ni L, Dainis A, Jenkins A, Regna K, Muskavitch M, Garrity P.
650 2012 Modulation of TRPA1 thermal sensitivity enables sensory discrimination in Drosophila. *Nature*
651 **481**, 76-81.

652 [20] Liu L, Li Y, Wang R, Yin C, Dong Q, Hing H, Kim C, Welsh MJ. 2007 Drosophila hygrosensation
653 requires the TRP channels water witch and nanchung. *Nature* **450**, 294-298. (10.1038/nature06223).

654 [21] Hamada FN, Rosenzweig M, Kang K, Pulver SR, Ghezzi A, Jegla TJ, Garrity PA. 2008 An
655 internal thermal sensor controlling temperature preference in Drosophila. *Nature* **454**, 217-220.
656 (10.1038/nature07001).

657 [22] Zhong L, Bellemer A, Yan H, Honjo K, Robertson J, Hwang Richard Y, Pitt Geoffrey S, Tracey
658 WD. 2012 Thermosensory and Nonthermosensory Isoforms of *Drosophila melanogaster*TRPA1
659 Reveal Heat-Sensor Domains of a ThermoTRP Channel. *Cell Reports* **1**, 43-55.
660 (10.1016/j.celrep.2011.11.002).

661 [23] Guntur A, Gy P, Takle K, Chen J, Yang X, Yang C-H. 2015 Drosophila TRPA1 isoforms detect
662 UV light via photochemical production of H2O2. *Proc Natl Acad Sci* **E5753-E5761**.

663 [24] Gu P, Gong J, Shang Y, Wang F, Ruppell KT, Ma Z, Sheehan AE, Freeman MR, Xiang Y. 2019
664 Polymodal Nociception in Drosophila Requires Alternative Splicing of TrpA1. *Curr Biol* **29**, 3961-
665 3973.e3966. (10.1016/j.cub.2019.09.070).

666 [25] Wang G, Qiu YT, Lu T, Kwon H-W, Jason Pitts R, Van Loon JJA, Takken W, Zwiebel LJ. 2009
667 *Anopheles gambiae* TRPA1 is a heat-activated channel expressed in thermosensitive sensilla of
668 female antennae. *European Journal of Neuroscience* **30**, 967-974. (10.1111/j.1460-
669 9568.2009.06901.x).

670 [26] Survery S, Moparthi L, Kjellbom P, Hogestatt E, Zygmunt PM, Johanson U. 2016 The N-terminal
671 Ankyrin Repeat Domain Is Not Required for Electrophile and Heat Activation of the Purified Mosquito
672 TRPA1 Receptor.

673 [27] Sato A, Sokabe T, Kashio M, Yasukochi Y, Tominaga M, Shiomi K. 2014 Embryonic
674 thermosensitive TRPA1 determines transgenerational diapause phenotype of the silkworm, Bombyx
675 mori. *Proc Natl Acad Sci U S A* **111**, E1249-1255. (10.1073/pnas.1322134111).

676 [28] Kohno K, Sokabe T, Tominaga M, Kadowaki T. 2010 Honey Bee Thermal/Chemical Sensor,
677 AmHsTRPA, Reveals Neofunctionalization and Loss of Transient Receptor Potential Channel
678 Genes. *The Journal of Neuroscience* **30**, 12219.

679 [29] Wang X, Li T, Kashio M, Xu Y, Tominaga M, Kadowaki T. 2018 HsTRPA of the Red Imported
680 Fire Ant, *Solenopsis invicta*, Functions as a Nocisensor and Uncovers the Evolutionary Plasticity of
681 HsTRPA Channels. *eNeuro* **5**, ENEURO.0327-0317.2018. (10.1523/ENEURO.0327-17.2018).

682 [30] Wigglesworth V. 1939 *The Principles of Insect Physiology (7 hardback editions; paperback*
683 *edition 1984)*. London, UK, Methuen and Co., Ltd.

684 [31] Coura JR, Viñas PA. 2010 Chagas disease: a new worldwide challenge. *Nature* **465**, S6-S7.
685 (10.1038/nature09221).

686 [32] 2015 Chagas disease in Latin America: an epidemiological update based on 2010 estimates.
687 *Wkly Epidemiol Rec* **90**, 33-43.

688 [33] WHO. 2002 Control of Chagas disease : second report of the World Health Organization (WHO)
689 expert committee. (World Health Organization.

[34] Clayton J. 2010 Chagas disease 101. *Nature* **465**, S4-S5. (10.1038/nature09220).

[35] Ceccarelli S, Balsalobre A, Medone P, Cano ME, Gurgel Gonçalves R, Feliciangeli D, Vezzani D, Wisnivesky-Colli C, Gorla DE, Marti GA, et al. 2018 DataTri, a database of American triatomine species occurrence. *Scientific data* **5**, 180071-180071. (10.1038/sdata.2018.71).

[36] Wigglesworth B, Gillett J. 1934 The function of the antennae in *Rhodnius prolixus* (Hemiptera) and the mechanism of orientation to the host. *J. Exp. Biol* **11**, 120-138.

[37] Mesquita RD, Vionette-Amaral RJ, Lowenberger C, Rivera-Pomar R, Monteiro FA, Minx P, Spieth J, Carvalho AB, Panzera F, Lawson D, et al. 2015 Genome of *Rhodnius prolixus*, an insect vector of Chagas disease, reveals unique adaptations to hematophagy and parasite infection. *Proceedings of the National Academy of Sciences* **112**, 14936-14941.

[38] Barrozo R, Reisenman C, Guerenstein P, Lazzari C, Lorenzo MG. 2016 An inside look at the sensory biology of triatomines. *Journal of Insect Physiology* **97**, 3-19. (doi: 10.1016/j.jinsphys.2016.11.003).

[39] Lazzari CR, Núñez J. 1989 The response to radiant heat and the estimation of the temperature of distant sources in Triatoma infestans. *Journal of Insect Physiology* **35**, 525-529.

[40] Lazzari CR, Nunez J. 1989 Blood temperature and feeding-behavior in triatoma infestans (heteroptera: Reduviidae). *Entomologia Generalis* **14**, 183-188.

[41] Guerenstein PG, Lazzari CR. 2009 Host-seeking: How triatomines acquire and make use of information to find blood. *Acta tropica* **110**, 148-158. (10.1016/j.actatropica.2008.09.019).

[42] Zopf L, Lazzari C, Tichy H. 2014 Differential effects of ambient temperature on warm cell responses to infrared radiation in the bloodsucking bug Rhodnius prolixus. *Journal of Neurophysiology* **111**, 1341-1349.

[43] Zopf L, Lazzari C, Tichy H. 2014 Infrared detection without specialized infrared receptors in the bloodsucking bug *Rhodnius prolixus*. *Journal of Neurophysiology* **112**, 1606.

[44] Latorre-Estivalis JM, Robertson HM, Walden KKO, Ruiz J, Gonçalves LO, Guarneri AA, Lorenzo MG. 2017 The molecular sensory machinery of a Chagas disease vector: expression changes through imaginal moult and sexually dimorphic features. *Scientific Reports* **7**, 40049. (10.1038/srep40049).

[45] Latorre-Estivalis JM, Lorenzo MG. 2019 Molecular bases of sensory processes in kissing bugs, vectors of Chagas disease. *Current Opinion in Insect Science* **34**, 80-84. (10.1016/j.cois.2019.03.010).

[46] Latorre-Estivalis JM, Sterkel M, Ons S, Lorenzo MG. 2020 Transcriptomics supports local sensory regulation in the antenna of the kissing-bug Rhodnius prolixus. *BMC Genomics* **21**, 101. (10.1186/s12864-020-6514-3).

[47] Chaverra-Rodriguez D, Macias VM, Hughes GL, Pujhari S, Suzuki Y, Peterson DR, Kim D, McKeand S, Rasgon JL. 2018 Targeted delivery of CRISPR-Cas9 ribonucleoprotein into arthropod ovaries for heritable germline gene editing. *Nature Communications* **9**, 3008. (10.1038/s41467-018-05425-9).

[48] Pereira J, Diogo C, Fonseca A, Bomfim L, Cardoso P, Santos A, Dittz U, Miranda K, de Souza W, Gioda A, et al. 2020 Silencing of RpATG8 impairs the biogenesis of maternal autophagosomes in vitellogenic oocytes, but does not interrupt follicular atresia in the insect vector *Rhodnius prolixus*. *PLOS Neglected Tropical Diseases* **14**, e0008012. (10.1371/journal.pntd.0008012).

[49] Neely GG, Keene AC, Duchek P, Chang EC, Wang Q-P, Aksoy YA, Rosenzweig M, Costigan M, Woolf CJ, Garrity PA, et al. 2011 TrpA1 Regulates Thermal Nociception in Drosophila. *PLOS ONE* **6**, e24343. (10.1371/journal.pone.0024343).

[50] Cattaneo AM, Bengtsson JM, Montagné N, Jacquin-Joly E, Rota-Stabelli O, Salvagnin U, Bassoli A, Witzgall P, Anfora G. 2016 TRPA5, an ankyrin subfamily insect TRP channel, is expressed in antennae of *Cydia pomonella* (Lepidoptera: Tortricidae) in multiple splice variants. *Journal of Insect Science* **16**, 83-83. (10.1093/jisesa/iew072).

[51] Jumper J, Evans R, Pritzel A, Green T, Figurnov M, Ronneberger O, Tunyasuvunakool K, Bates R, Zidek A, Potapenko A, et al. 2021 Highly accurate protein structure prediction with AlphaFold. *Nature* **596**, 583-589. (doi:10.1038/s41586-021-03819-2).

[52] Varadi M, Anyango S, Deshpande M, Nair S, Natassia C, Yordanova G, Yuan D, Stroe O, Wood G, Laydon A, et al. 2021 AlphaFold Protein Structure Database: massively expanding the structural coverage of protein-sequence space with high-accuracy models. *Nucleic Acids Research* **50**, D439-D444. (10.1093/nar/gkab1061).

[53] Mirdita M, Schutze K, Moriwaki Y, Heo L, Ovchinnikov S, Steinegger M. 2022 ColabFold: making protein folding accessible to all. *Nat Methods* **19**, 679-682. (10.1038/s41592-022-01488-1).

[54] Paulsen CE, Armache JP, Gao Y, Cheng Y, Julius D. 2015 Structure of the TRPA1 ion channel suggests regulatory mechanisms. *Nature* **520**, 511-517. (10.1038/nature14367).

[55] Wang X, Li Y, Wei H, Yang Z, Luo R, Gao Y, Zhang W, Liu X, Sun L. 2023 Molecular architecture and gating mechanisms of the Drosophila TRPA1 channel. *Cell Discov* **9**, 36. (10.1038/s41421-023-00527-1).

[56] Zhao J, Lin King JV, Paulsen CE, Cheng Y, Julius D. 2020 Irritant-evoked activation and calcium modulation of the TRPA1 receptor. *Nature*. (10.1038/s41586-020-2480-9).

[57] Gaudet R. 2008 A primer on ankyrin repeat function in TRP channels and beyond. *Molecular bioSystems* **4**, 372-379. (10.1039/b801481g).

[58] Ladrón-de-Guevara E, Dominguez L, Rangel-Yescas GE, Fernández-Velasco DA, Torres-Larios A, Rosenbaum T, Islas LD. 2020 The Contribution of the Ankyrin Repeat Domain of TRPV1 as a Thermal Module. *Biophys J* **118**, 836-845. (10.1016/j.bpj.2019.10.041).

[59] Zheng W, Qin F. 2015 A combined coarse-grained and all-atom simulation of TRPV1 channel gating and heat activation. *J Gen Physiol* **145**, 443-456. (10.1085/jgp.201411335).

[60] Cordero-Morales JF, Gracheva EO, Julius D. 2011 Cytoplasmic ankyrin repeats of transient receptor potential A1 (TRPA1) dictate sensitivity to thermal and chemical stimuli. *Proceedings of the National Academy of Sciences* **108**, E1184.

[61] Moparthi L, Survery S, Kreir M, Simonsen C, Kjellbom P, Högestätt ED, Johanson U, Zygmunt PM. 2014 Human TRPA1 is intrinsically cold- and chemosensitive with and without its N-terminal ankyrin repeat domain. *Proc Natl Acad Sci U S A* **111**, 16901-16906. (10.1073/pnas.1412689111).

[62] Liénard M, Bernard GD, Allen A, Lassance J, Song S, Childers R, Yu N, Ye D, Stephenson A, Valencia-Montoya W, et al. 2021 The evolution of red colour vision is linked to coordinated rhodopsin tuning in lycaenid butterflies. *PNAS* **118** e2008986118. (doi.org/10.1073/pnas.2008986118).

[63] Yao J, Liu B, Qin F. 2010 Kinetic and energetic analysis of thermally activated TRPV1 channels.

[64] Caterina MJ, Schumacher MA, Tominaga M, Rosen TA, Levine JD, Julius D. 1997 The capsaicin receptor: a heat-activated ion channel in the pain pathway. *Nature* **389**, 816-824. (10.1038/39807).

[65] Liu B, Qin F. 2017 Single-residue molecular switch for high-temperature dependence of vanilloid receptor TRPV3. *Proc Natl Acad Sci U S A* **114**, 1589-1594. (10.1073/pnas.1615304114).

[66] Latorre R, Brauchi S, Orta G, Zaelzer C, Vargas G. 2007 ThermoTRP channels as modular proteins with allosteric gating. *Cell Calcium* **42**, 427-438.

[67] Baez D, Raddatz N, Ferreira G, Gonzalez C, Latorre R. 2014 Chapter Three - Gating of Thermally Activated Channels. In *Current Topics in Membranes* (eds. L. D. Islas & F. Qin), pp. 51-87, Academic Press.

[68] Caterina MJ, Julius D. 2001 The Vanilloid Receptor: A Molecular Gateway to the Pain Pathway. *Annual Review of Neuroscience* **24**, 487-517. (10.1146/annurev.neuro.24.1.487).

[69] Güler A, Lee H, Lida T, Shimizu I, Tominaga M, Caterina M. 2002 Heat-evoked activation of the ion channel, TRPV4.

[70] Smith GD, Gunthorpe MJ, Kelsell RE, Hayes PD, Reilly P, Facer P, Wright JE, Jerman JC, Walhin JP, Ooi L, et al. 2002 TRPV3 is a temperature-sensitive vanilloid receptor-like protein. *Nature* **418**, 186-190. (10.1038/nature00894).

[71] Diver MM, Lin King JV, Julius D, Cheng Y. 2022 Sensory TRP Channels in Three Dimensions. *Annu Rev Biochem* **91**, 629-649. (10.1146/annurev-biochem-032620-105738).

[72] Laursen WJ, Anderson EO, Hoffstaetter LJ, Bagriantsev SN, Gracheva EO. 2015 Species-specific temperature sensitivity of TRPA1.

[73] Tsai C-C, Childers RA, Nan Shi N, Ren C, Pelaez JN, Bernard GD, Pierce NE, Yu N. 2020 Physical and behavioral adaptations to prevent overheating of the living wings of butterflies. *Nature Communications* **11**, 551. (10.1038/s41467-020-14408-8).

[74] Schmitz H, Trenner S, Hofmann MH, Bleckmann H. 2000 The ability of *Rhodnius prolixus* (Hemiptera; Reduviidae) to approach a thermal source solely by its infrared radiation. *Journal of Insect Physiology* **46**, 745-751.

[75] Flores GB, Lazzari CR. 1996 The role of the antennae in Triatoma infestans: Orientation towards thermal sources. *Journal of Insect Physiology* **42**, 433-440. (doi.org/10.1016/0022-1910(95)00137-9).

[76] Ferreira RA, Lazzari CR, Lorenzo MG, Pereira MH. 2007 Do Haematophagous Bugs Assess Skin Surface Temperature to Detect Blood Vessels? *PLOS ONE* **2**, e932. (10.1371/journal.pone.0000932).

[77] Zermoglio PF, Latorre-Estivalis JM, Crespo JE, Lorenzo MG, Lazzari CR. 2015 Thermosensation and the TRPV channel in Rhodnius prolixus. *Journal of Insect Physiology* **81**, 145-156. (doi.org/10.1016/j.jinsphys.2015.07.014).

[78] Voets T, Talavera K, Owsianik G, Nilius B. 2005 Sensing with TRP channels. *Nature Chemical Biology* **1**, 1-8.

[79] Yin C, Shen G, Guo D, Wang S, Ma X, Xiao H, Liu J, Zhang Z, Liu Y, Zhang Y, et al. 2015 InsectBase: a resource for insect genomes and transcriptomes. *Nucleic Acids Research* **44**, D801-D807. (10.1093/nar/gkv1204).

[80] Thurmond J, Goodman JL, Strelets VB, Attrill H, Gramates L S, Marygold SJ, Matthews BB, Millburn G, Antonazzo G, Trovisco V, et al. 2018 FlyBase 2.0: the next generation. *Nucleic Acids Research* **47**, D759-D765. (10.1093/nar/gky1003).

[81] Elsik CG, Tayal A, Diesh CM, Unni DR, Emery ML, Nguyen HN, Hagen DE. 2015 Hymenoptera Genome Database: integrating genome annotations in HymenopteraMine. *Nucleic Acids Research* **44**, D793-D800. (10.1093/nar/gkv1208).

[82] Altschul SF, Madden TL, Schäffer AA, Zhang J, Zhang Z, Miller W, Lipman DJ. 1997 Gapped BLAST and PSI-BLAST: a new generation of protein database search programs. *Nucleic Acids Research* **25**, 3389-3402.

[83] Poelchau M, Childers C, Moore G, Tsavatapalli V, Evans J, Lee C-Y, Lin H, Lin J-W, Hackett K. 2014 The i5k Workspace@NAL—enabling genomic data access, visualization and curation of arthropod genomes. *Nucleic Acids Research* **43**, D714-D719. (10.1093/nar/gku983).

[84] Emms D, Kelly S. 2019 OrthoFinder: phylogenetic orthology inference for comparative genomics. *Genome Biology* **20**, 238. (doi:10.1186/s13059-019-1832-y).

[85] Katoh K, Standley D. 2013 MAFFT Multiple sequence alignment software version 7: improvements in performance and usability. *Mol Biol Evol* **30**, 772-780. (doi:10.1093/molbev/mst010).

[86] Nguyen L-T, Schmidt HA, von Haeseler A, Minh BQ. 2015 IQ-TREE: A fast and effective stochastic algorithm for estimating maximum likelihood phylogenies. *Mol Biol Evol* **32**, 268-274.

[87] Trifinopoulos J, Nguyen L-T, von Haeseler A, Minh BQ. 2016 W-IQ-TREE: a fast online phylogenetic tool for maximum likelihood analysis. *Nucleic Acids Research* **44**, W232-W235. (10.1093/nar/gkw256).

[88] Kalyaanamoorthy S, Minh BQ, Wong TK, von Haeseler A, Jermiin LS. 2017 ModelFinder: Fast model selection for accurate phylogenetic estimates. *Nature Methods* **14**, 587-589.

[89] Yu G. 2020 Using ggtree to Visualize Data on Tree-Like Structures. *Current Protocols in Bioinformatics* **69**, e96. (10.1002/cpbi.96).

[90] Zhang H, Gao S, Lercher M, Hu S, Chen W-H. 2012 EvolView, an online tool for visualizing, annotating and managing phylogenetic trees. *Nucleic Acids Res* **40**, W569-W572.

[91] Martin M. 2011 Cutadapt removes adapter sequences from high-throughput sequencing reads. *2011* **17**, 3. (10.14806/ej.17.1.200).

[92] Kim D, Paggi JM, Park C, Bennett C, Salzberg SL. 2019 Graph-based genome alignment and genotyping with HISAT2 and HISAT-genotype. *Nature Biotechnology* **37**, 907-915. (10.1038/s41587-019-0201-4).

[93] Pertea M, Pertea GM, Antonescu CM, Chang TC, Mendell JT, Salzberg SL. 2015 StringTie enables improved reconstruction of a transcriptome from RNA-seq reads. *Nat Biotechnol* **33**, 290-295. (10.1038/nbt.3122).

[94] Bryant DM, Johnson K, Tia D, Tickle T, Couger MB, Payzin-Dogru D, Lee T, Leigh N, Kuo T, ., et al. 2017 A Tissue-Mapped Axolotl De Novo Transcriptome Enables Identification of Limb Regeneration Factors. *Cell rep* **18**, 762-776.

[95] Lee E, Helt GA, Reese JT, Munoz-Torres MC, Childers CP, Buels RM, Stein L, Holmes IH, Elsik CG, Lewis SE. 2013 Web Apollo: a web-based genomic annotation editing platform. *Genome Biology* **14**, R93. (10.1186/gb-2013-14-8-r93).

[96] Soneson C, Matthes KL, Nowicka M, Law CW, Robinson MD. 2016 Isoform prefiltering improves performance of count-based methods for analysis of differential transcript usage. *Genome Biology* **17**, 12. (10.1186/s13059-015-0862-3).

[97] Kearse M, Moir R, Wilson A, Stones-Havas S, Cheung M, Sturrock S, Buxton S, Cooper A, Markowitz S, Duran C, et al. 2012 Geneious Basic: An integrated and extendable desktop software platform for the organization and analysis of sequence data. *Bioinformatics* **28**, 1647-1649.

[98] The PyMOL Molecular Graphics System, Version 1.8, Schrödinger, LLC. (

863 [99] Holm L. 2020 DALI and the persistence of protein shape. *Protein Sci* **29**, 128-140.
864 (10.1002/pro.3749).

865 [100] Liénard MA, Valencia-Montoya WA, Pierce NE. 2022 Molecular advances to study the
866 function, evolution and spectral tuning of arthropod visual opsins. *Philosophical Transactions of the*
867 *Royal Society B: Biological Sciences* **377**. (doi:10.1098/rstb.2021.0279).

868 [101] Yao J, Liu B, Qin F. 2009 Rapid Temperature Jump by Infrared Diode Laser Irradiation for
869 Patch-Clamp Studies. *Biophysical Journal* **96**, 3611-3619.

870

871 **Extended data**

Convergent evolution of noxious heat sensing by TRPA5, a novel class of heat sensor in *Rhodnius prolixus*

872 **Marjorie A. Liénard[1,2,3*], David Baez-Nieto[4*], Cheng-Chia Tsai[5], Wendy A. Valencia-Montoya[2], Balder**

873 **Werin[6], Urban Johanson[6], Jean-Marc Lassance[2,7], Jen Q. Pan[4], Nanfang Yu[5], Naomi E. Pierce[2]**

874 [1]Department of Biology, Lund University, Lund, Sweden

875 [2]Department of Organismic and Evolutionary Biology and Museum of Comparative Zoology, Harvard University,
876 Cambridge, MA 02138, USA

877 [3]Broad Institute, Cambridge, MA 02142, USA

878 [4]Stanley Center for Psychiatric Research, Broad Institute, Cambridge, MA 02142, USA

879 [5]Department of Applied Physics and Applied Mathematics, Columbia University, New York, NY 10027, USA

880 [6]Division of Biochemistry and Structural Biology, Department of Chemistry, Lund University, Lund, Sweden

881 [7]GIGA-Research, University of Liège, Liège, Belgium

882 **This document contains:**

883 **Supplementary Methods**

884 **Supplementary Figures S1 to S8**

885 **SI Tables S1 to S5 are in a separate file**

Supplementary Methods

PID control

A PID (proportional-integral-derivative) control is the typical way to adjust the output according to the input reading in real-time without knowing most of the environmental parameters. The idea is described in the following function:

$$Output(t) = K_p Err(t) + K_i \int_0^t Err(\tau)d\tau + K_d \frac{dErr(t)}{dt}$$

$$Err(t) = Input(t) - Setpoint$$

with $Output(t)$ being the laser power, $Input(t)$ being the temperature, and $Setpoint$ being the desired value. The $Output(t)$ is determined by $Err(t)$, which is the difference between $Input(t)$ and $Setpoint$.

There are 3 terms in this equation, the first term is the proportional term. This term varies linearly with $Err(t)$. For instance, when the temperature reaches the setpoint, this term decreases, and when the temperature exceeds the setpoint, this term becomes negative to bring the temperature back to the setpoint.

The second term is the integral term. This term provides a gradually increasing offset and this offset will stabilize when the temperature stabilizes to setpoint, where $Err(t) \to 0$.

The third term is the derivative term. This term estimates the required change of output by watching the inertia of $Err(t)$. For instance, when the temperature reaches the setpoint, the proportional term gives 0 and the integral term gives a stabilized value, but if the temperature is still increasing, this term will decrease the output to prevent the temperature from exceeding the setpoint in the next time interval.

Open pipette current measurements

The temperature is measured by monitoring the current through an open patch pipette, which means there are no cells but only water, assuming the thermal property of the cell is the same as water. First, a series of open-pipette measurements with different laser powers and power waveforms is performed and used to calculate the

temperature evolution from real-time current in the patch-clamp recording pipette. The patch-clamp experiment is conducted by applying the same laser powers and waveforms to the cell (Fig. S4)

Fiber preparation

The attenuation coefficient of water at the wavelength of 1460 nm is ~3000 cm^(−1) which means the absorption of the laser power through a 100nm thick water layer is over 40%. Using the fiber above the water surface, the laser would thus deliver most of its power in the upper water layer. The temperature of water above the targeted cell would be much higher than the cell temperature itself, and the temperature change would not be confined to a single cell due to conduction and convection in the water. To resolve this, we cut the fiber with a diamond blade under a stereomicroscope and stripped the fiber which allowed us to place the fiber tip in the water layer directly above the cell in the recording chamber (Fig. S5). The relative position of the fiber tip and cell was adjusted using patch-clamp rig microscope.

Supplementary Figures

Figure S1. Phylogeny of insect TRPA channels

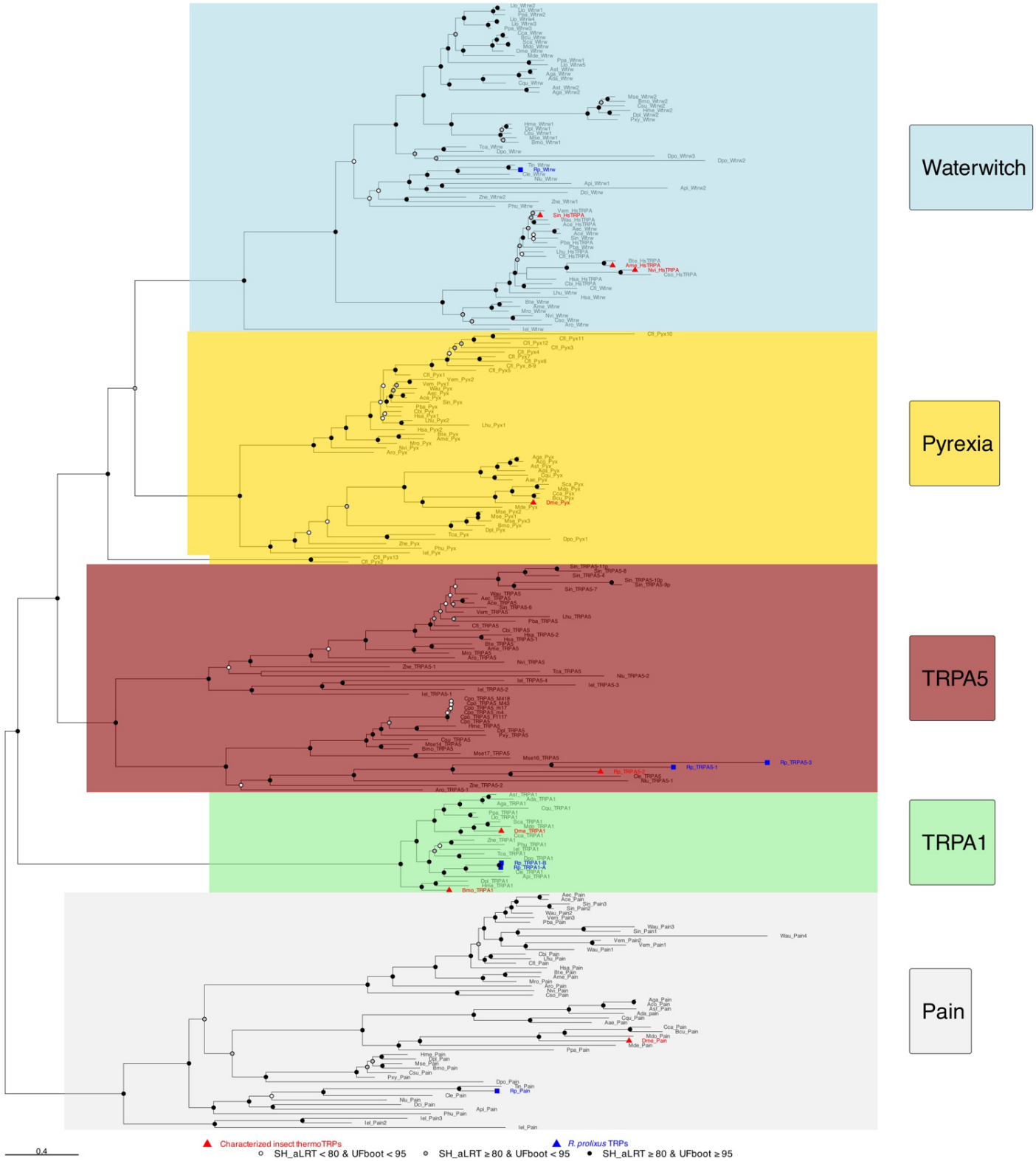

Figure S1. Phylogeny of insect TRPA channels. The Maximum-likelihood phylogeny of amino acid sequences includes representative ion channel members of the TRPA1, Pain, Pyrexia, HsTRPA, TRPA5, Wtw subfamilies. Accession numbers are listed in Table S1. The tree was inferred in IQ-TREE v1.6.11 using ModelFinder, Ultrafast Bootstrap (UFboot), 1000 replicates, using a best-fit model JTT+F+I+G4 measured by the Bayesian information criterion (BIC). Branches were assigned Shimodaira-Hasegawa approximate likelihood ratio test (SH-aLRT) and UFboot supports. The tree was visualized in Rstudio (2021.09.2) using ggtree (Script provided). Species represented are **Anoplura**: *Pediculus humanus* (Phu, head louse), **Coleoptera**: *Tribolium castaneum* (Tca, red flour beetle), *Dendroctonus ponderosae* (Dpo, Mountain pine beetle), *Photynus pyralis* (Ppy, Common Eastern Firefly), *Agrilus planipennis* (Apl, Emerald ash borer), *Anoplophora glabripennis* (All, Asian longhorned beetle), *Aethina tumida* (Aut, Small hive beetle), *Onthophagus taurus* (Ota, bull dung beetle), **Diptera**: *Drosophila melanogaster* (Dme, fruitfly), *Mayetiola destructor* (Mde, Hessian fly), *Culex quinquefasciatus* (Cqu, Southern house mosquito), *Anopheles stephensi* (Ast), *Anopheles gambiae* (Aga), *Anopheles darlingi* (Ada), *Bactrocera cucurbitae* (Bcu, Melon fly), *Ceratitis capitata* (Cca, Mediterranean fruit fly), *Musca domestica* (Mdo, housefly), *Lutzomyia longipalpis (Llo, Sandfly), Phlebotomus papatasi* (Ppa, Sandfly), *Stomoxys calcitrans* (Sca, Barn fly), **Hemiptera:** *Acyrthosiphon pisum* (Api, pea aphid), *Nilaparvata lugens* (Nlu, Brown planthopper), *Diaphorina citri* (Dci, Asiatic citrus psyllid), *Cimex lectularius* (Cle, Bed bug), *Triatoma infestans* (Tin, Winchuka) *Rhodnius prolixus* (Rp, Kissing bug), **Hymenoptera:** *Apis mellifera* (Ame, Western honeybee) , *Bombus terrestris* (Bte, Buff-tailed bumblebee), *Megachile rotundata* (Mro, Alfalfa leaf cutting bee), *Nasonia vitripenis* (Nvi, Jewel wasp), *Harpegnathos saltator* (Hsa, Jumping ant), *Linepithema humile* (Lhu, Argentine ant), *Campanatus floridanus* (Cfl, Florida carpenter ant), *Pogonomyrmex barbatus* (Pba, red harvester ant), *Atta cephalotes* (Ace, Leafcutter ant), *Acromyrmex echinatior* (Aec, Panamian leafctutter ant), *Solenopsis invicta* (Sin, Red imported fire ant), *Vollenhovia emeryi* (Vem, ant), *Athalia rosae* (Aro, Turnip sawfly), *Cerapachys biroi* (Cbi, Clonal raider ant), *Ceratosolen solmsi* (Cso, Fig wasp), *Wasmannia auropunctata* (Wau, Electric ant), **Isoptera:** *Zootermopsis nevadensis* (Zne, Dampwood termite), **Lepidoptera**: *Bombyx mori* (Bmo, Silkmoth), *Chilo suppressalis* (Csu, Asiatic rice borer), *Danaus plexippus* (Dpl, Monarch butterfly), *Heliconius melpomene* (Hme, Postman butterfly), *Plutella xylostella* (Diamondback moth), *Manduca sexta* (Mse, Tobacco hornworm) *Cydia pomonella* (Cpo, Codling moth), **Odonata**: *Ischnura elegans* (Iel, Bluetail damselfly).

950 **Figure S2. Phylogeny of insect TRPA5 channels**

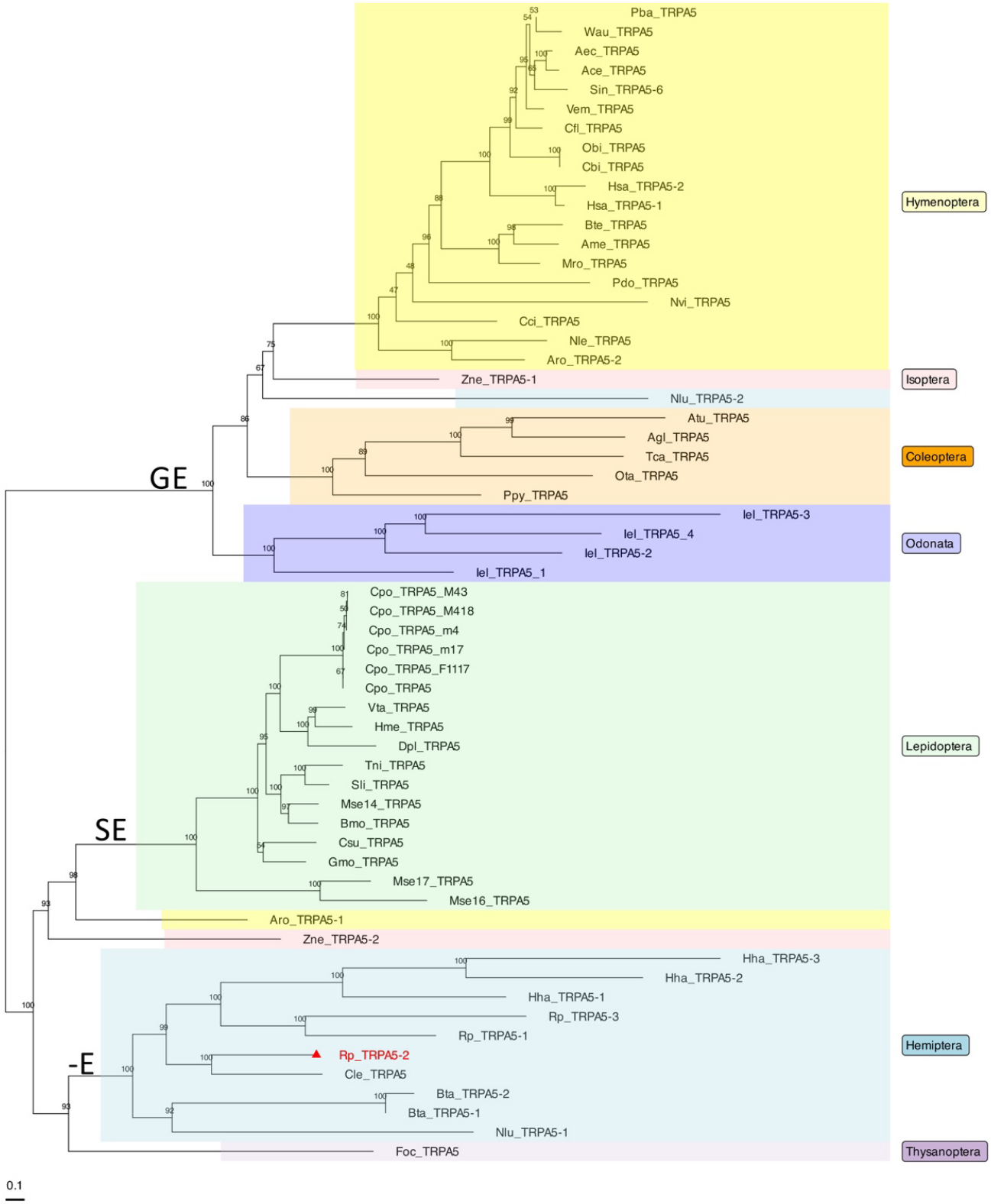

951

Figure S2. Phylogeny of insect TRPA5 channels. TRPA5 channels are present across insect Orders but Diptera. The Maximum-likelihood phylogeny of amino acid sequences includes representative ion channel members of the TRPA5 subfamily. The tree was inferred in IQ-TREE v1.6.11 using ModelFinder, Ultrafast Bootstrap (UFboot), 1000 replicates, using a best-fit model JTT+F+I+G4 measured by the Bayesian information criterion (BIC). Branches were assigned Shimodaira-Hasegawa approximate likelihood ratio test (SH-aLRT) and UFboot supports. The tree was visualized in Rstudio (2021.09.2) using ggtree (script provided). Species abbreviations are as follows: **Coleoptera:** *Tribolium castaneum* (Tca, red flour beetle), *Photynus pyralis* (Ppy, Common Eastern Firefly), *Anoplophora glabripennis* (Agl, Asian longhorned beetle), *Aethina tumida* (Aut, Small hive beetle), *Onthophagus taurus* (Ota, bull dung beetle); **Hemiptera**: *Bemisia tabaci* (Bta, Silverleaf Whitefly), *Cimex lectularius* (Cle, Bed bug), *Halyomorpha halys* (Hha, Brown marmorated stinkbug), *Nilaparvata lugens* (Nlu, Brown planthopper), *Rhodnius prolixus* (Rp, Kissing bug); **Hymenoptera**: *Apis mellifera* (Ame, Western honeybee) , *Athalia rosae* (Aro, Turnip sawfly), *Bombus terrestris* (Bte, Buff-tailed bumblebee), *Megachile rotundata* (Mro, Alfalfa leaf cutting bee), *Nasonia vitripennis* (Nvi, Jewel wasp), *Harpegnathos saltator* (Hsa, Jumping ant), *Linepithema humile* (Lhu, Argentine ant), *Campanatus floridanus* (Cfl, Florida carpenter ant), *Pogonomyrmex barbatus* (Pba, red harvester ant), *Atta cephalotes* (Ace, Leafcutter ant), *Acromyrmex echinatior* (Aec, Panamian leafcutter ant), *Solenopsis invicta* (Sin, Red imported fire ant), *Vollenhovia emery* (Vem, ant), *Ooceraea biroi* (Cbi, Clonal raider ant), *Wasmannia auropunctata* (Wau, Electric ant), *Polisted dominula* (Pdo, European paper wasp), *Neodiprion lecontei* (Nle, Red-headed pine sawfly), *Cephus cinctus* (Cci, Wheat stem sawfly); **Isoptera**: *Zootermopsis nevadensis* (Zne, Dampwood termite); **Lepidoptera:** *Bombyx mori* (Bmo, Silkmoth), *Chilo suppressalis* (Csu, Asiatic rice borer), *Danaus plexippus* (Dpl, Monarch butterfly), *Heliconius melpomene* (Hme, Postman butterfly), *Plutella xylostella* (Pxy, Diamondback moth), *Manduca sexta* (Mse, Tobacco hornworm), *Cydia pomonella* (Cpo, Codling moth), *Vanessa tameamea* (Vta, Kamehameha butterfly), *Trichoplusia ni* (Tni, Cabbage looper), *Spodoptera litura* (Sli, Tobacco cutworm), *Galleria mellonella* (Gmo, Greater wax moth), **Odonata**: *Ischnura elegans* (Iel, damselfly), **Thysanoptera**: *Frankliniella occidentalis* (Foc, thrips). Capital letters above branches represent the amino acid residues at the ion channel selectivity filter (see Fig. 2).

978 **Figure S3. qCPR analysis**

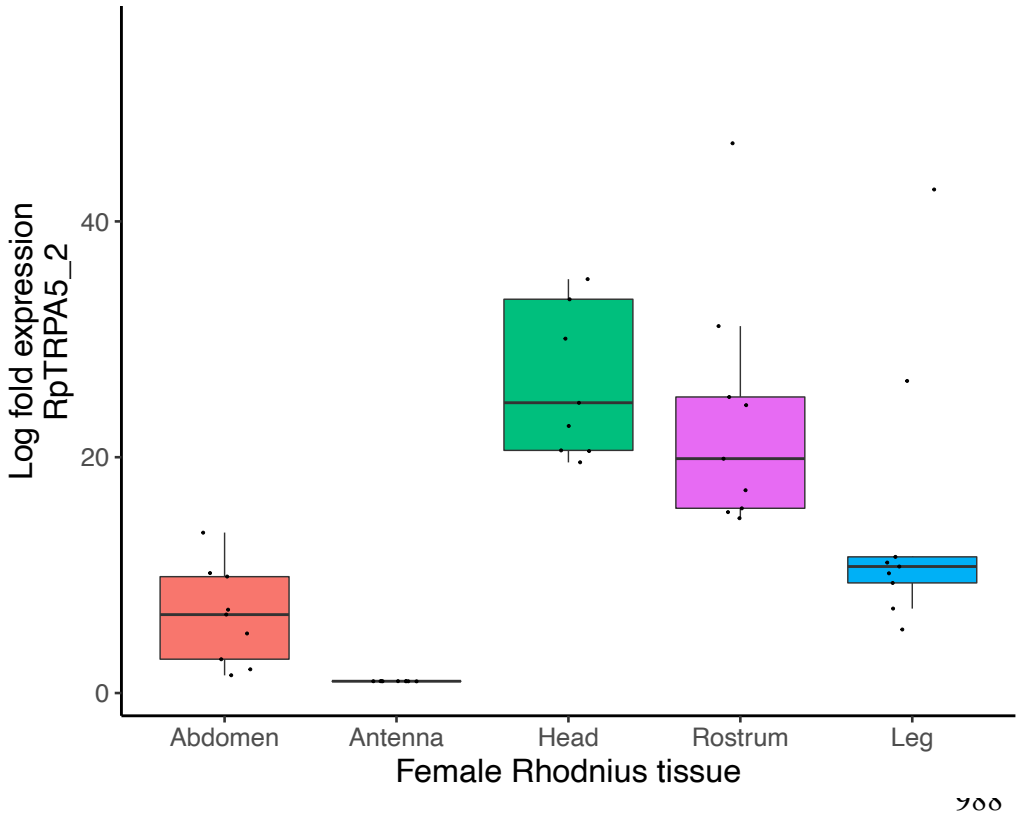

989 **Figure S3.** Differential expression pattern of Rp-TRPA5$_2$ transcripts isolated from *R. prolixus* female sensory
990 tissues and monitored by quantitative PCR. The mean relative expression scores were calculated from raw cycle
991 threshold (Ct) values (±SEM, n= 9) (Table S5) and boxplots were visualized in R (script provided). Log$_2$ fold
992 change expression values are shown relative to the *Rhodnius* housekeeping gene (Actin) and calibrated to
993 expression in Antenna.

994 **Fig. S4. DALI Analysis**

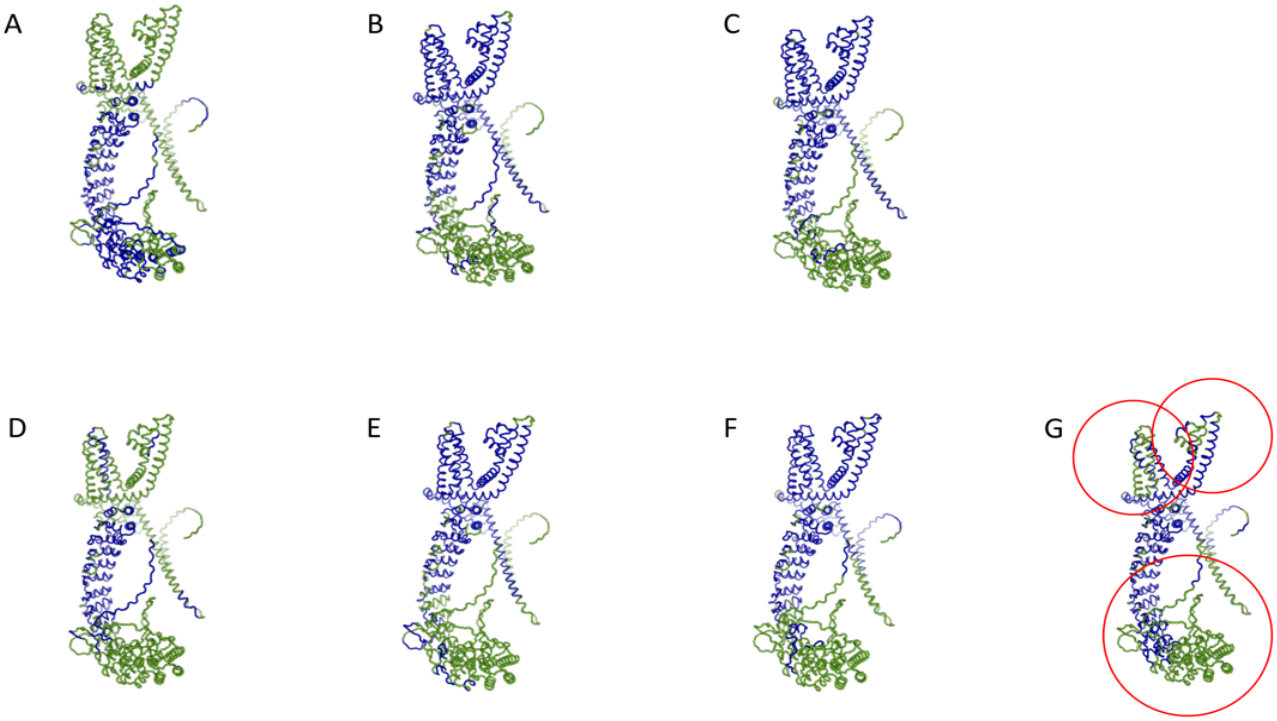

995

996 **Figure S4. DALI Analysis.** Pairwise structural alignment using the Dali server
997 (http://ekhidna2.biocenter.helsinki.fi/dali/), of different monomers against Rhodnius $TRPA5_2$. **A.** Rhodnius
998 TRPA1, **B**. Rhodnius Painless, **C.** Rhodnius Waterwitch, **D.** Drosophila TRPA1, **E.** Drosophila Painless, **F.**
999 Drosophila Waterwitch, **G.** Drosophila Pyrexia. The red circles in **G** indicate areas where the Pyrexia monomer
1000 stands out in that the pore region and the voltage sensor domain are less similar to $TRPA5_2$, but the ARD is
1001 more similar to $TRPA5_2$.

Figure S5. TRP whole cell and surface expression.

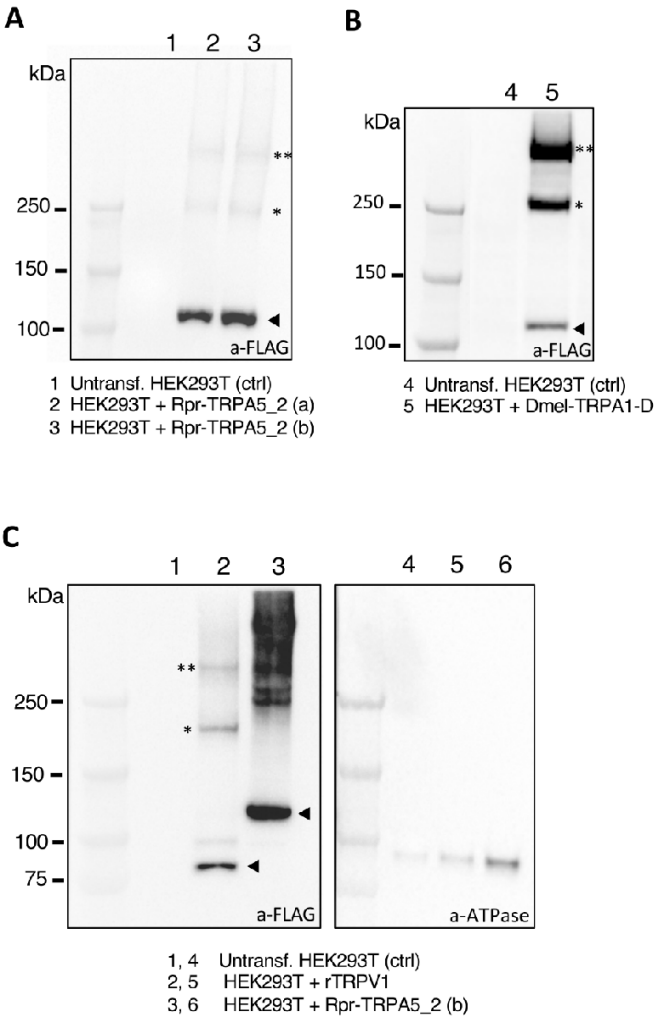

Figure S5. A-B. **Rp-TRPA5$_2$ anti-FLAG signals in whole cell lysates**. Untransfected HEK293T cells (lanes 1,4) and HEK293T cells transfected with 2.5 µg pcDNA-FLAG-T2A-mRuby plasmid DNAs for Rp-TRPA5$_2$ (A, lanes 2,3), and fruitly Dmel-TRPA1-D (B, lane 5). Cells were collected 72 hrs after transfection. The protein ladder image taken from the same membrane is juxtaposed to the left of the immunoblot. One and two asterisks represent predicted dimeric and tetrameric TRP forms, respectively. The predicted monomeric MW is indicated with a black arrowhead: Rp-TRPA5$_2$, 127.78 kDa; fruit fly Dmel-TRPA1-D 138.82 kDa. **C.** Surface expression analysis of Rp-TRPA5$_2$. Biotinylated surface protein eluates were run in parallel wells on the same SDS-page gel to probe TRP (left) and ATPase (right). Anti-FLAG levels in surface protein fraction are from non-transfected HEK293T cells (lane 1), cells expressing rTRPV1 (lane 2), and cells expressing Rp-TRPA5$_2$ (lane 3). Lanes 4 to 6 are the corresponding anti-ATPase biotin-surface fraction from non-transfected HEK293T cells (lane 4), cells expressing rTRPV1 (lane 5), and cells expressing Rp-TRPA5$_2$ (lane 6). One and two asterisks represent predicted dimeric and tetrameric TRP forms, respectively. The predicted monomeric MW is indicated with a black arrowhead (rTRPV1, 94.95 kDa; Rp-TRPA5$_2$, 127.78 kDa).

Figure S6. Schematics of the functional assay workflow and optical fiber-patch clamp recording setup

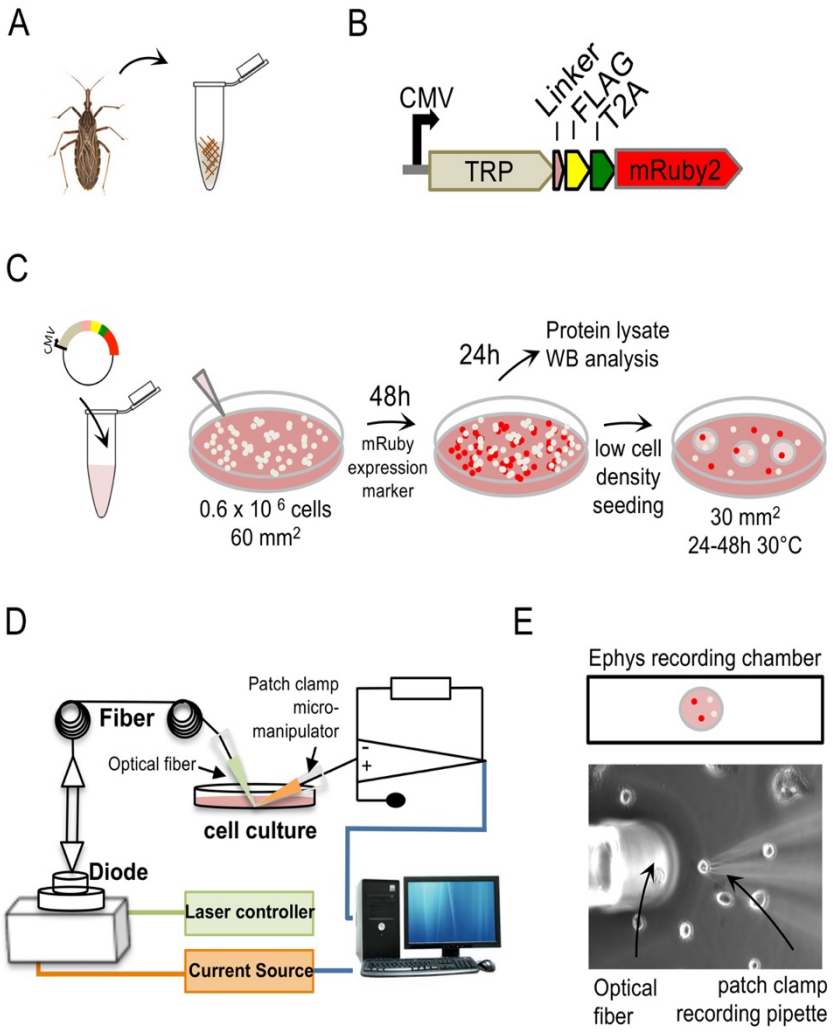

Figure S6. Schematic drawing of the experimental workflow used to characterize *Rhodnius prolixus* thermo TRPA5$_2$ ion channel. A. The full TRPA5$_2$ ORF sequence was amplified from *Rhodnius prolixus* antenna and gene-specific primers, sequenced-verified, then codon-optimized for mammalian expression, and subcloned in a custom-made pFRT-TO-FLAG-T2A-mRuby2 expression cassette under expression of the CMV promoter (1) **(B)**. **C**. HEK293T cells seeded at low density were transiently transfected with plasmid DNA-lipid complexes and incubated at 37°C for 48h to allow TRP surface membrane expression. Monomeric mRuby2 fluorescent protein (mRuby2) was co-expressed as a cytoplasmic marker. 48h post-transfection, cells were prepared for patch-clamp recording by seeding in a 30-mm^2 culture dish overlaid with round glass cover slips. Cells were incubated at 30°C. **D**. Electrophysiology recordings took place after 24h to 48h using an optical fiber-based setup adapted after Yao et al 2009 (2), designed to couple manual patch clamp recordings with fiber optics as a mean to provide controllable optical and thermal stimulations to individual cells expressing candidate thermosensitive receptor proteins. The setup consists of a fiber launch system combining a high-power optical fiber tuned to near-infrared wavelengths (λc =1460 nm (+/-20 nm), Po= 4.8 watts), a visible alignment laser (red), and a laser

diode controller, forming a PID control loop using the patch clamp current as the feedback signal. **E**. During the experiment, a laser spot is aligned with one single patched cell (see Fig. S8) stably expressing the membrane receptor protein of interest in the cover slip placed in the recording chamber.

1034 **Figure S7. Validation with rTRPV1 and Dm-TRPA1-D**

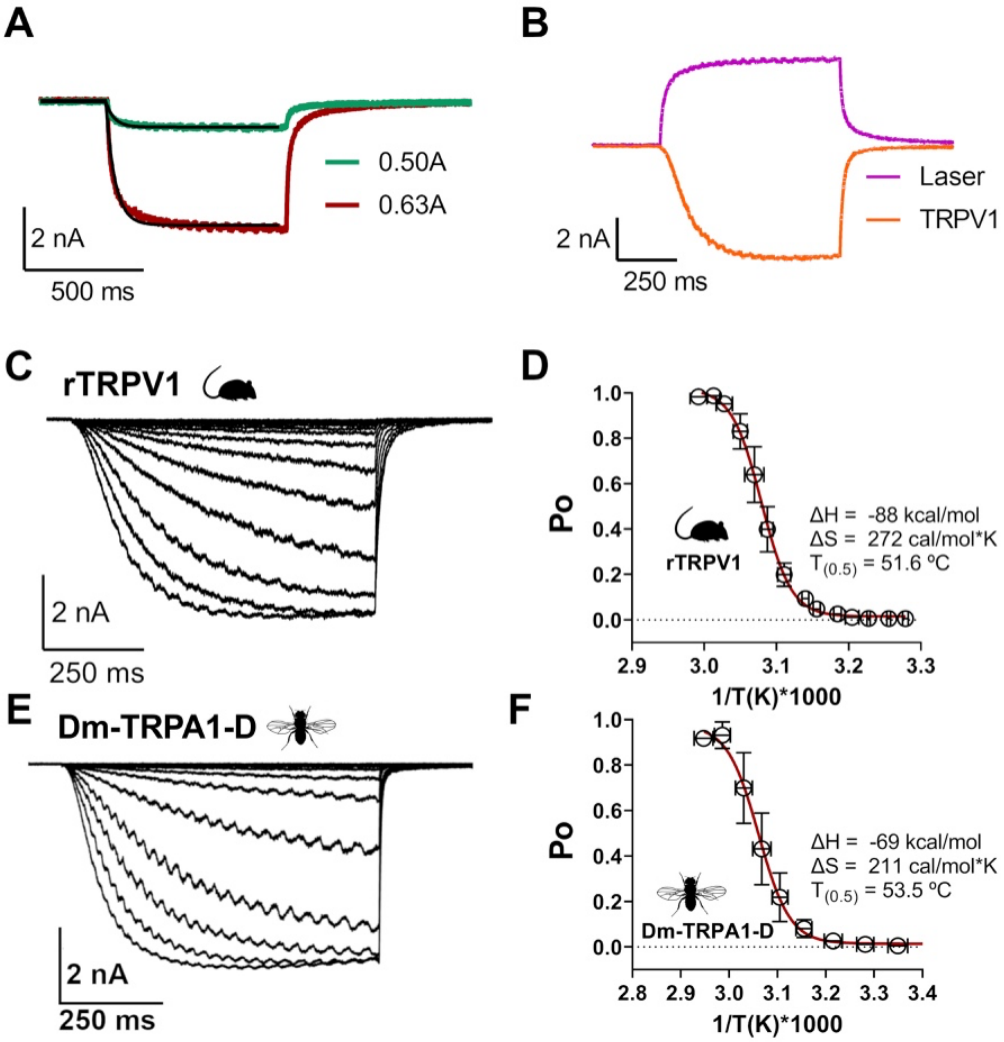

1035 **Figure S7. Validation with rTRPV1 and Dm-TRPA1-D**. **A.** Time course of the ionic current through the open
1036 pipette at -10 mV holding voltage when a current of 0.50A (green trace) and 0.63A (red trace) was applied to the
1037 laser diode. The temperature jumps for those currents correspond to 32.1°C and 59.7°C, from 22.6°C,
1038 respectively. Both temperature jumps can be fitted by a mono-exponential function with a time constant of ~35
1039 ms (black line). **B.** Time course comparison between the current through the open pipette (magenta trace) and
1040 a HEK293T cell expressing rTRPV1 channels under voltage clamp at -30 mV (orange trace), in response to a
1041 temperature jump from 22.6°C to 59.7°C (0.63A). The current through rTRPV1 channels is three times slower
1042 than the laser kinetics with a time constant of ~100 ms. **C.** Representative heat-activated current traces of a
1043 HEK293T cell expressing rTRPV1 under voltage clamp (holding voltage of -30 mV). The currents were elicited
1044 by temperature jumps from room temperature (22.6°C) up to 59.7°C with a duration of 700 ms. **D.** Fraction of
1045 rTRPV1 channels in the open state (Open probability, Po) as a function of the temperature. The Po vs 1/T was
1046 fitted to a Boltzman function (red line) with the midpoint of activation ($T_{0.5}$) reached at 51.6°C. The Van't Hoff plot

estimates for rTRPV1 provides an activation enthalpy of the endothermic transition at 88.3±9.4 kcal/mol and an entropic change associated to the temperature activation process at 271±28 cal/mol*K. at -30 mV as a function of the temperature. These values in our new expression cassette are very close to previously published values of ΔH = 85 kcal/mol, $T_{0.5}$ = 45.6°C (2,3). **E.** Representative heat-activated current traces of a HEK293 cell expressing Dm-TRPA1-D channels under voltage clamp (holding voltage of -30 mV). The currents were elicited by temperature jumps from room temperature (19.4°C) up to 63.5°C with a duration of 700 ms. **F.** Fraction of Dm-TRPA1-D channels in the open state (Open probability, Po) as a function of the temperature. The Po vs 1/T was fitted to a Boltzman function (red line) with the midpoint of activation ($T_{0.5}$) reached at 53.5°C, the Van't Hoff plot estimates for Dm-TRPA1-D an activation enthalpy of the endothermic transition at 68.7±13.1 kcal/mol and an entropic change associated to the temperature activation process at 211±40 cal/mol·K at -30 mV. The stationary current at the end of the temperature pulse (last 100 ms) was used to calculate all the thermodynamics parameters. Data are presented as means ± standard deviation.

Figure S8.

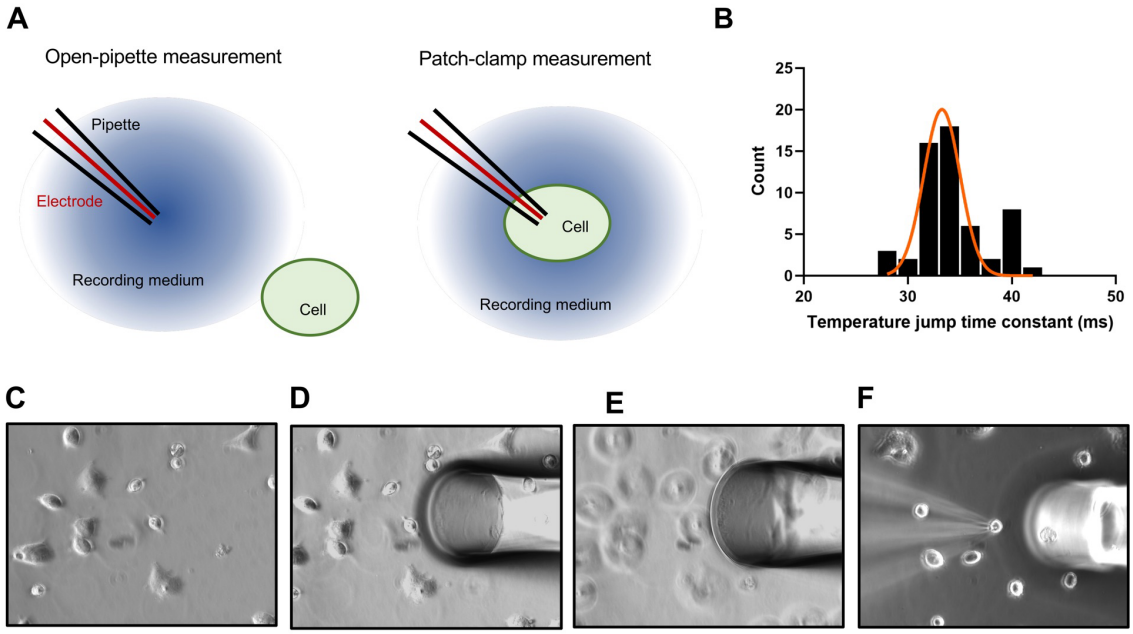

Figure S8. Open pipette temperature calibration and optic fiber positioning prior to each cell patch clamp experiment A. Schematic representation of open pipette temperature calibration. First the open pipette is positioned under the center of the laser using the reference marks on the screen. Then we proceed to record the current through the open pipette elicited as a function of a series of near IR laser pulses. With these current traces we can estimate the temperature jumps magnitude that will be applied later to the target cell. After this the target cell is positioned in the center of the laser beam using the microscope stage translation (the optic fiber stays fixed). Once the cell is in the right position, we use the same pipette used for the calibration to carry out the electrophysiological recording, applying the same set of pulses used in the calibration **B.** Histogram of the time constants from the exponential fit to the open pipette current traces from the temperature jumps used in the rTRPV1 experiments (n=56), the mean time constant was 33.3±1.8 ms. **C.** View of HEK293T cells seeded at low density on a glass cover in the recording chamber on the patch-clamp rig station. **D.** After finding a target cell co-expressing mRuby2 as a fluorescent marker (see Fig. 1B), with the help of an automatized micromanipulator, the optic fiber is placed in the recording solution using the reference marks on the computer screen (not shown here) defined during the calibration with the visible laser. The depth in the solution is adjusted so that the fiber is directly above a single cell in the recording medium. **E.** The field of view is changed to align the patch clamp electrode to the reference marks. **F.** The target cell expressing mRuby2 is patched with the recording electrode, now visible on the left side, whereas the fiber is directly above the target cell. The relative position between the recording pipette and the fiber was established using a visible laser during the setup of the system, and is constant for all the experiments.

Extended data References

(1) Liénard MA, Valencia-Montoya WA, Pierce NE. 2022 Molecular advances to study the function, evolution and spectral tuning of arthropod visual opsins. *Philosophical Transactions of the Royal Society B: Biological Sciences 377.* (doi:10.1098/rstb.2021.0279).

(2) Yao J, Liu B, Qin F. 2010 Kinetic and energetic analysis of thermally activated TRPV1 channels. *Biophys J* 99, 1743-1753. (10.1016/j.bpj.2010.07.022).

(3) Liu B, Hui K,Qin F. 2003 Thermodynamics of Heat Activation of Single Capsaicin Ion Channels VR1 *Biophys J.* 85(5): 2988–3006. (10.1016/S0006-3495(03)74719-5)